Electrified thin film flow at finite Reynolds number on planar substrates featuring topography

S. Veremieiev[a,*], H.M. Thompson[a], M Scholle[b],
Y.C. Lee[c], P.H. Gaskell[a]

August 18, 2015

[a] School of Mechanical Engineering, University of Leeds, Leeds, LS2 9JT, UK
[b] Institute for Automotive Technology and Mechatronics, Heilbronn University, 74081 Heilbronn, Germany
[c] Department of Mechanical Engineering, Heriot-Watt University, Edinburgh, EH14 4AS, UK

Abstract

The flow of a gravity-driven thin liquid film over a substrate containing topography, in the presence of a normal electric field, is investigated. The liquid is assumed to be a perfect conductor and the air above it a perfect dielectric. Of particular interest is the interplay between inertia, for finite values of the Reynolds number, Re, and electric field strength, expressed in terms of the Weber number, We, on the resultant free-surface disturbance away from planarity. The hydrodynamics of the film are modelled via a depth-averaged form of the Navier-Stokes equations which is coupled to a Fourier series separable solution of Laplace's equation for the electric potential: detailed steady-state solutions of the coupled equation set are obtained numerically.

The case of two-dimensional flow over different forms of discrete and periodically varying spanwise topography is explored. In the case of the familiar free-surface capillary peaks and depressions that arise for steep topography, and become more pronounced with increasing Re, greater electric field strength affects them differently. In particular, it is found that for topography heights commensurate with the long-wave approximation: (i) the capillary ridge associated with a step-down topography at first increases before decreasing, both monotonically, with increasing We; (ii) the free-surface hump which arises at a step-up topography continues to increase monotonically with increasing We, the increase achieved being smaller the larger the value of Re.

A series of results for the more practically relevant problem of three-dimensional film flow over substrate containing a localised square trench topography is provided. These exhibit behaviour and features consistent with those observed for two-dimensional flow, in that as We is increased the primary free-surface capillary ridges and depressions are at first enhanced, with a corresponding narrowing, before becoming suppressed. In addition, it is found that, while the well-known horse-shoe shaped disturbance characteristic of such flows continues to persist with increasing Re in the absence of an electric field, when the latter is present and We increased in value the associated comet tail disappears as does the related downstream surge. The phenomenon is explained with reference to the competition between the corresponding capillary pressure and Maxwell stress distributions.

Keywords: Thin liquid films; Free surface flow; Inertia; Electrohydrodynamics; Numerical solutions; Topography

* Corresponding author. Tel.: +44 1133432200; fax: +44 1132424611. E-mail address: s.veremieiev@leeds.ac.uk (S. Veremieiev).

1 Introduction

The many roles and relevance of thin liquid films, whether they occur naturally or feature/arise as part of a particular engineering, technological or scientific application, is exemplified in the recent comprehensive review of Craster and Matar (2009). The principal challenge in relation to modelling such problems is the need to account for the presence of a bounding free surface, the location of which is not known a priori. It is no surprise, therefore, that much of the progress historically has centered on the solution of the idealised two-dimensional problem: it is in recent years only that significant inroads have been made into solving a certain class of three-dimensional flows. Of particular interest over the past two decades or so, has been a variety of problems associated with thin film flow on substrates containing topography - either randomly occurring and discrete (Peurrung and Graves 1993; Decré and Baret 2003; Gaskell, Jimack, Sellier, Thompson and Wilson 2004; Veremieiev, Thompson, Lee and Gaskell 2010), or periodically repeating (Vlachogiannis and Bontozoglou 2002; Wierschem, Scholle and Aksel 2003, Wierschem and Aksel 2004). From an industrial standpoint these types of flow are important in: the manufacture of micro-scale sensors and devices, Tabeling (2005); the coating of paper, plastics and metals, Kistler and Schweizer (1997); heat exchanger design, Helbig, Nasarek, Gambaryan-Roisman and Stephan (2009); the performance of vaporisation turbine combustion chambers, Helbig, Alexeev, Gambaryan-Roisman and Stephan (2005); the production of electronic components such as displays and printed circuits, Decré and Baret (2003).

Arguably the practical overarching goal apropos the above, is to minimise the free-surface disturbance that arises, in order to yield optimum performance in terms of, for example, heat and mass transfer (Yoshimura, Nosoko and Nagata 1996; Serifi, Malamataris and Bontozoglou 2004), and evaporation (Gaskell, Jimack, Sellier and Thompson, 2006), or to maximise free-surface planarity in manufacturing applications to ensure predictable functional or optical properties (Stillwagon and Larson 1988, 1990). To this end, thermally-induced Marangoni stresses, Gramlich, Kalliadasis, Homsy and Messer (2002), viscoelastic fluid behaviour, Saprykin, Koopmans and Kalliadasis (2007), and selective topography design, Sellier (2008) and Heining and Aksel (2009), have each been suggested recently as a means of controlling the degree of free-surface disturbance generated. The use of electric fields, on the other hand, for manipulating the behaviour of thin liquid films stretches back several decades, having been investigated by various authors with particular applications in mind. In industrial coating processes, for example, electric fields are combined with charge distributions at the substrate to create electrostatic assist, thus widening the coating window by controlling the position of the associated dynamic wetting line in order to avoid/postpone the onset of air entrainment, Nakajima and Miyamoto (1993). In addition, electric fields have been used to increase the micro-mixing of fluids (Oddy, Santiago and Mikkelsen, 2001), in the context of electrostatic liquid film radiators (Bankoff, Miksis, Gwinner and Kim, 1994; Bankoff, Griffing and Schluter, 2002) and to create patterns on films (Schäffer, Thurn-Albrecht, Russel and Steiner, 2000; Craster and Matar, 2005; Wu, Pease and Russell, 2005). They have similarly been utilised for the manipulation of droplets (Yeo, Craster and Matar, 2007), and to align droplets in a particular direction (Mahlmann and Papageorgiou, 2009).

Of late Tseluiko, Blyth, Papageogiou and Vanden-Broeck (2008a, 2008b) have considered the effects of substrate topography on steady, two-dimensional electrified film flow at zero Reynolds number. They addressed gravity-driven Stokes flow over a sinusoidally corrugated surface, with comparisons drawn between predictions from lubrication theory for small amplitude corrugations against boundary element solutions valid for corrugations and trench topography of arbitrary size. The latter solutions were used to confirm the range of applicability of the lubrication

analysis and to investigate the conditions under which eddies are generated adjacent to wavy topography. For the case of flow past trench topography it was shown that an electric field can either reduce or promote irregularities at the film surface, depending on the local geometry and the electrical properties of the film: for one which is a perfect conductor/(dielectric) the height of the capillary ridge upstream of the trench was found to decrease/(increase) monotonically as the electric field strength increased. A related long-wave analysis was carried out for flow over an inclined surface containing periodic steps, trenches and mound indentations with the liquid film assumed to be a perfect conductor and the air above it a perfect dielectric. This work revealed that an electric field, applied normal to the film, is able to eliminate the capillary ridge at a step-down topography at the expense of creating a free-surface hump at an adjacent step-up one. These analyses were subsequently extended to consider, in a limited sense, the additional influence of inertia in determining the free-surface shape for the case of a perfect dielectric film flowing over a wavy wall, Tseluiko and Blyth (2009).

The above theoretical electrohydrodynamic analyses are directed at two-dimensional, spanwise flows only; the investigation of three-dimensional ones having yet to appear. The principal reason for this is that the computational resources required to obtain, ideally, a full and accurate numerical solution of the three-dimensional Navier-Stokes equations governing the free-surface flow problem, even without the added complexity of having to solve accompanying coupled electric field equations, remains a major hurdle and is why simpler hydrodynamic models have been employed in the main. Solving the Navier-Stokes or Stokes equations, subject to the attendant boundary conditions, using a finite or boundary element method would, however, overcome many of the restrictions associated with models based on the long-wave approximation - namely removing the constraint on choice of Capillary number, film thickness or topography aspect ratio. The boundary element method has been used widely to study two-dimensional Stokes flows over topography (Pozrikidis, 1988; Mazouchi and Homsy, 2001). It has found limited application in the case of three-dimensional flows, (Pozrikidis and Thoroddsen, 1991; Luo and Pozrikidis, 2006, 2007; Blyth and Pozrikidis, 2006); see also the work of Baxter, Power, Cliffe and Hibberd (2009, 2010) concerning the gravity-driven flow of thin films around obstacles. Finite element solutions of the full Navier-Stokes equations, on the other hand, for non-zero Reynolds number have been restricted to the case of steady-state two-dimensional flow. Bontozoglou and Serifi (2008), for example, explored the free-surface disturbance generated by film flow down a vertical plane containing an isolated step topography, showing that for large Capillary numbers increasing inertia first amplifies and then diminishes the capillary features. The reader's attention is directed also to the investigations of Trifonov (1999), Malamataris and Bontozogolou (1999) and Gu, Liu, Yan and Yu (2004); the latter finding good agreement with the experimental work of Zhao and Cerro (1992). Recently, Scholle, Haas, Aksel, Wilson, Thompson and Gaskell (2008a) considered the subtleties associated with the competing effects of geometry and inertia on the underpinning local flow structure in thick-gravity driven films on sinusoidally varying substrate. In addition, good agreement was found, in the limit of Stokes-like flow, with corresponding experimental data and flow visualisations reported by Wierschem et al (2003); see also their related work on eddy genesis and manipulation (Scholle, Haas, Aksel, Wilson, Thompson and Gaskell, 2009) together with the effect of the same on global heat transfer (Scholle, Haas, Aksel, Thompson, Hewson and Gaskell, 2008b) in plane laminar shear flow, the study of Wierschem, Pollack, Heining and Aksel (2010) concerned with eddy suppression in film flow over topography and the investigation of Nguyen and Bontozoglou (2011) directed at inertial film flow along strongly undulated substrates.

Returning to the adoption of a long-wave approximation, the three-dimensional predictions obtained by Gaskell et al (2004) using an accurate numerical solution strategy, were the first of their kind to appear and found to agree extremely well with the benchmark experimental

data of Decré and Baret (2003). Indeed, not only was lubrication theory shown to produce accurate results in regions of parameter space where it is not strictly valid, the authors were able to quantify the expected error in terms of Reynolds number and topography height/depth by a detailed comparison with complementary finite element solutions of the full Navier-Stokes equations for the case of spanwise topography. Veremieiev et al (2010) recently considered the same problem; this time undertaking a detailed investigation of the effect of inertia using a model based on depth-averaging the governing unsteady Navier-Stokes equations, a method akin to the integral boundary layer approximation developed by Shkadov (1967, 1968) for flow over flat substrates and subsequently utilised for the case when surface topography is present by Trifonov (2004) and Saprykin et al (2007). Not only were they able to isolate and identify the role of inertia, the results obtained lend further support to the suitability of the long-wave approximation for resolving gravity-driven flows when the topography depth/height to film thickness ratio is sufficiently small and the Reynolds number is not too large.

No review would be complete without reference to the related issue of the hydrodynamic stability of film flows. Benjamin (1957) and Yih (1963) have shown, in the case of two-dimensional, gravity-driven flow down a flat inclined substrate, there exists a critical Reynolds number beyond which the flow becomes unstable to long waves, see also Chang (1994): a result that has been verified experimentally by Liu, Paul and Gollub (1993) and Liu and Gollub (1994). Complementary numerical investigations of waves at the surface of a flowing film have been reported by Ramaswamy, Chippada and Joo (1996) and Malamataris, Vlachogiannis and Bontozoglou (2002). With particular reference to the influence of electric fields on flow stability, it has long been known that instabilities can be induced by applying a sufficiently strong electric field across a film (Melcher and Taylor,1969; González and Castellanos, 1996). For gravity-driven, two-dimensional film flow down flat inclined substrates, Kim, Bankoff and Miksis (1992) showed that the presence of an electric field normal to it lowers the critical Reynolds number at which free-surface instability occurs. Several subsequent studies have carried out stability analyses of this problem using the long-wave approximation where the additional Maxwell stress term in the free-surface stress boundary condition is obtained by the solution of the associated two-dimensional Laplace equation for the electric potential. The work of Tseluiko and Papageorgiou (2006a, 2006b), for example, showed that applying an electric field normal to a film can excite a long-wave instability even at zero Reynolds number. Such findings have been confirmed experimentally by Griffing, Bankoff, Miksis and Schluter (2006), whose complementary lubrication predictions of the dynamical effect of a strong normal electric field agree reasonably well with their data.

In contrast, comparatively few studies have appeared that consider the combined influences of inertia and topography on the stability of thin films and none have emerged that consider also the presence of an electric field. Recent experiments, however, in which the flow is taken to be essentially two-dimensional in a streamwise cross-sectional plane, have demonstrated that there is a strong coupling between inertia and topography for the case of gravity-driven flow over surfaces containing spanwise periodic rectangular (Vlachogiannis and Bontozoglou, 2002; Argyriadi, Vlachogiannis and Bontozoglou, 2006) or wavy (Wierschem, Lepski and Aksel, 2005) features. The experimentally-observed rise in critical Reynolds number with increasing topography steepness that occurs has also been predicted theoretically by several authors, see for example Wierschem and Aksel (2003), Trifonov (2007) and Dávalos-Orozco (2007, 2008); conversely, it has been reported recently that undulating surfaces may have a destabilising influence on the flow if the surface tension is sufficiently high (Heining and Aksel, 2009; D'Alessio, Pascal and Jasmine, 2009; Häcker and Uecker 2009).

The present work has two main strands in relation to gravity-driven film flow at finite Reynolds number in the presence of an electric field normal to it: two-dimensional flow over dis-

crete steep and smooth periodically varying spanwise topography revisited; three-dimensional flow over localised steep topography, the exploration of which is considered for the first time. In both cases, the hydrodynamics is modelled using the approach of Veremieiev et al (2010) and the governing equation set solved numerically. Solution of the coupled three-dimensional Laplace equation for the electric potential is obtained in the form of a Fourier series in separable variables. In all cases the results obtained are compared and contrasted in detail with those of previous studies, where they exist. In the case of two-dimensional flow in the absence of an electric field, corresponding finite element solutions of the Navier-Stokes equations reveal both the underlying flow structure and the limitations associated with approximate models for inertia utilised within a standard lubrication framework.

2 Problem formulation

The problem of interest, see Figure 1, is that of steady, gravity-driven thin film flow down a planar substrate containing topography, shown for illustrative purposes as a discrete trench, of depth S_0, streamwise length L_T and spanwise width W_T; a uniform electric field, of strength, E_0, is applied normal to the substrate which is inclined at an angle $\theta \neq 0$ to the horizontal, with the liquid taken to be incompressible, having constant density, ρ, viscosity, μ, and surface tension, σ. The Cartesian streamwise, X, spanwise, Y, and normal, Z, coordinates are as indicated and the solution domain bounded from below by the substrate, $Z = S(X, Y)$, from above by the free surface, $Z = F(X, Y)$, by an upstream inflow condition at $X = 0$, together with far-field conditions at the outflow, $X = L_p$, and to the left and right at $Y = 0$ and $Y = W_p$, respectively. The film thickness at any point in the (X, Y) plane is given by $H = F - S$.

The liquid is assumed to be perfectly conducting, so that there is no electric field inside it and no potential difference between the substrate and the free surface; the air above it has comparatively negligible viscosity, is taken to be stationary and assumed to be an ideal dielectric with constant electrical permittivity, ε_e. This prescription is valid for fluids with high electrical conductivity, such as liquid metals or liquid electrolytes with high levels of impurity. The electric field, $\boldsymbol{E}$, is related to the electric potential, Φ, via $\boldsymbol{E} = -\nabla\Phi$. The resulting laminar flow is governed by the steady Navier-Stokes and continuity equations, namely:

$$\rho\left(\boldsymbol{U}\cdot\nabla\boldsymbol{U}\right) = -\nabla P + \nabla\cdot\boldsymbol{T} + \rho\boldsymbol{G}, \tag{1}$$

$$\nabla\cdot\boldsymbol{U} = 0, \tag{2}$$

while the electric potential in the air above the film satisfies Laplace's equation:

$$\nabla^2\Phi = 0. \tag{3}$$

In equations (1) and (2), $\boldsymbol{U} = (U, V, W)$ and P are the fluid velocity and pressure, respectively; $\boldsymbol{T} = \mu\left(\nabla\boldsymbol{U} + (\nabla\boldsymbol{U})^T\right)$ is the viscous stress tensor; $\boldsymbol{G} = G_0\left(\sin\theta, 0, -\cos\theta\right)$ is the acceleration due to gravity with G_0 the standard gravity constant. Without loss of generality, Φ is given the value zero at both the substrate, $Z = S(X, Y)$, and the free surface, $Z = F(X, Y)$.

The fluid flow and electric field equations are coupled via the free-surface stress boundary condition:

$$\left(-P\boldsymbol{I} + \boldsymbol{T}\right)|_{Z=F}\cdot\boldsymbol{n} = \left(\sigma K\boldsymbol{I} + P_A\boldsymbol{I} + \boldsymbol{M}|_{Z=F}\right)\cdot\boldsymbol{n}, \tag{4}$$

where $\boldsymbol{M} = \varepsilon_e\left(\boldsymbol{E}\otimes\boldsymbol{E} - \frac{1}{2}\boldsymbol{E}^2\boldsymbol{I}\right)$ is the Maxwell stress tensor acting on the surface of a conductor; $\otimes$ denotes the dyadic product of two vectors; $\boldsymbol{I}$ is the unity tensor; $\boldsymbol{n} = \left(-\frac{\partial F}{\partial X}, -\frac{\partial F}{\partial Y}, 1\right)\cdot\left[\left(\frac{\partial F}{\partial X}\right)^2 + \left(\frac{\partial F}{\partial Y}\right)^2 + 1\right]^{-1/2}$ is the unit normal vector pointing outward from the free surface;

$K = -\nabla \cdot \boldsymbol{n}$ is twice the mean curvature of the free surface that, following for example Saprykin et al (2007), is taken to be positive when the surface is concave upwards; P_A is the pressure of the surrounding air. In what follows the pressure variable is shifted, $P \to P + P_A$, to denote instead a reference pressure.

Taking the asymptotic, or fully-developed, film thickness, H_0, as a universal reference length-scale, the free-surface (maximum) velocity, $U_0 = \rho G_0 H_0^2 \sin\theta / 2\mu$, apropos the classic Nusselt solution (Spurk and Aksel, 2008) as an appropriate velocity-scale and scaling the pressure (stress tensor) via $P_0 = \mu U_0 / H_0$, equations (1) and (2) in non-dimensional form are:

$$\mathrm{Re}\,(\boldsymbol{u} \cdot \nabla \boldsymbol{u}) = -\nabla p + \nabla \cdot \boldsymbol{\tau} + \mathrm{St}\boldsymbol{g}, \tag{5}$$

$$\nabla \cdot \boldsymbol{u} = 0, \tag{6}$$

where $\boldsymbol{u} = (u, v, w)$, $\boldsymbol{\tau}$ and $\boldsymbol{g} = \boldsymbol{G}/G_0$ are dimensionless velocity, viscous stress tensor and gravity component, respectively; $\mathrm{Re} = \rho U_0 H_0 / \mu$ is the Reynolds number and $\mathrm{St} = \rho G_0 H_0^2 / \mu U_0 = 2/\sin\theta$ the Stokes number. Alternatively, the latter can be written in terms of the Froude number, $Fr = U_0 / \sqrt{H_0 G_0}$, as $\mathrm{St} = \mathrm{Re}/Fr^2$. The electric field is scaled by its magnitude E_0 and the electrical potential by $E_0 H_0$; equation (3) rewritten in terms of the dimensionless electrical potential, φ, is then:

$$\nabla^2 \varphi = 0. \tag{7}$$

Noting that an electric field is orientated normal to the surface of a conductor, Landau and Lifshitz (1984), namely:

$$\boldsymbol{e}|_{z=f} \cdot \boldsymbol{t} = 0, \tag{8}$$

the stress boundary condition (4) in non-dimensional form can be separated into normal and tangential components by taking its scalar product with respect to both the unit normal and tangent vectors at the free surface, that is:

$$-p|_{z=f} + (\boldsymbol{\tau}|_{z=f} \cdot \boldsymbol{n}) \cdot \boldsymbol{n} = \frac{\kappa}{\mathrm{Ca}} + \mathrm{We}\,(\nabla\varphi)^2\,|_{z=f}, \tag{9}$$

$$(\boldsymbol{\tau}|_{z=f} \cdot \boldsymbol{n}) \cdot \boldsymbol{t} = 0. \tag{10}$$

where $\boldsymbol{e}$ is the dimensionless electric field; $\mathrm{Ca} = \mu U_0 / \sigma$ is the Capillary number, the ratio of viscous to surface tension forces; $\mathrm{We} = \varepsilon_e H_0 E_0^2 / 2\mu U_0$, the Weber number, provides a measure of the relative importance of electrical to viscous forces. The unit vector tangential to the free surface is $\boldsymbol{t} = \left(\alpha_t, \beta_t, \alpha_t \frac{\partial f}{\partial x} + \beta_t \frac{\partial f}{\partial y}\right) \left[\alpha_t^2 + \beta_t^2 + \left(\alpha_t \frac{\partial f}{\partial x} + \beta_t \frac{\partial f}{\partial y}\right)^2\right]^{-1/2}$, where α_t and β_t are constants that define its direction at a point in the tangent plane; thus formula (10) actually implies two boundary conditions. Conditions (9) and (10) result in an important fact: the Maxwell stresses do not contribute to the tangential stress balance.

No-slip is imposed at the substrate:

$$\boldsymbol{u}|_{z=s} = 0, \tag{11}$$

together with the following kinematic constraint at the free surface:

$$\boldsymbol{u}|_{z=f} \cdot \boldsymbol{n} = 0. \tag{12}$$

Since equation (6) is satisfied for a film of arbitrary thickness over a flat substrate, in order to guarantee unique solutions it is necessary to specify an additional constraint for the film thickness, see Scholle et al (2008a). In the case of flow over a discrete trench or peak

topography located on a flat inclined substrate, the film thickness at the inflow boundary is imposed via:

$$h|_{x=0} = 1. \tag{13}$$

For the case of flow over periodically repeating, wavy substrates extending to the boundary, a boundary condition ensuring that the fixed volume of fluid involved is preserved is more appropriate; setting this as equivalent to the same volume of fluid flowing over a uniformly flat substrate, the same is enforced by requiring that:

$$\int_0^{l_p} \int_0^{w_p} h dx dy = l_p w_p. \tag{14}$$

In addition, the following condition on electric potential holds at the free surface:

$$\varphi|_{z=f} = 0, \tag{15}$$

and the imposition of a uniform electric field at infinity requires that:

$$\nabla\varphi|_{z\to\infty} = (0, 0, -1)\,. \tag{16}$$

The electrohydrodynamic problem is closed by imposing periodic boundary conditions in both x and y directions at the far-field extremities of the domain of interest:

$$(\boldsymbol{u}, p, h, s, \varphi)\,|_{x=l_p} = (\boldsymbol{u}, p, h, s, \varphi)\,|_{x=0}, \quad (\boldsymbol{u}, p, h, s, \varphi)\,|_{y=w_p} = (\boldsymbol{u}, p, h, s, \varphi)\,|_{y=0}. \tag{17}$$

In expressions (8)-(17), x, y, z, h, s, f, p and κ are the dimensionless values of their upper-case counterparts, as are s_0, l_t, w_t, l_p and w_p.

The complexity of the general flow problem as specified above can be reduced to one which is more tractable, while retaining the nonlinear inertial terms, by depth-averaging equations (5) and (6). Since the approach is described in detail elsewhere, Veremieiev et al (2010), an outline only is provided. In brief, the governing hydrodynamic equations and associated boundary conditions are simplified in terms of the long-wave approximation, Oron, Davis and Bankoff (1997), on the basis that the ratio $\varepsilon = H_0/L_0 \ll 1$, where $L_0 = (\sigma H_0/3\rho G_0 \sin\theta)^{1/3}$ is the characteristic in-plane capillary length scale, Gaskell et al (2004). The key steps involve:

(i) Re-scaling equations (5) - (6) and boundary conditions (9) - (14) in terms of L_0, which is equivalent to the following change of non-dimensional variables: $(x, y, l_t, w_t, l_p, w_p, p) \to (x, y, l_t, w_t, l_p, w_p, p)/\varepsilon$, $w \to \varepsilon w$ with all terms of $\mathrm{O}(\varepsilon^2)$ or higher neglected; the scalings used for the other variables remain unchanged.

(ii) Averaging the re-scaled equations over the depth of the thin film, $h = H/H_0$, and formulating them in terms of the averaged velocities $\bar{u}\,(x, y) = \frac{1}{h}\int_s^f u dz$, $\bar{v}\,(x, y) = \frac{1}{h}\int_s^f v dz$, the pressure $p\,(x, y, z)$ and the film thickness $h\,(x, y)$.

(iii) Specifying the unknown friction and dispersion terms appearing in the averaged equation set using the assumption that the velocity profiles across the film have the same and consistent self-similar form as the classical Nusselt solution:

$$u = 3\bar{u}\left(\xi - \frac{\xi^2}{2}\right), \quad v = 3\bar{v}\left(\xi - \frac{\xi^2}{2}\right), \quad \text{where } \xi = \frac{z - s}{h}. \tag{18}$$

Proceeding in this way yields the following depth-averaged form (DAF) equation set:

$$\frac{6}{5}\varepsilon \mathrm{Re}\left(\bar{u}\frac{\partial \bar{u}}{\partial x}+\bar{v}\frac{\partial \bar{u}}{\partial y}\right)=-\frac{\partial p}{\partial x}-\frac{3\bar{u}}{h^2}+2, \tag{19}$$

$$\frac{6}{5}\varepsilon \mathrm{Re}\left(\bar{u}\frac{\partial \bar{v}}{\partial x}+\bar{v}\frac{\partial \bar{v}}{\partial y}\right)=-\frac{\partial p}{\partial y}-\frac{3\bar{v}}{h^2}, \tag{20}$$

$$p=-\frac{\varepsilon^3}{\mathrm{Ca}}\nabla^2\left(h+s\right)+2\varepsilon\left(h+s-z\right)\cot\theta-\varepsilon \mathrm{We}\left(\frac{\partial \varphi}{\partial z}\right)^2|_{z=f}, \tag{21}$$

$$\frac{\partial (h\bar{u})}{\partial x}+\frac{\partial (h\bar{v})}{\partial y}=0, \tag{22}$$

which is solved subject to either constraint (13) or (14) and the following far-field periodic boundary conditions:

$$\left(\bar{u},\bar{v},p,h\right)|_{x=l_p}=\left(\bar{u},\bar{v},p,h\right)|_{x=0},\quad \left(\bar{u},\bar{v},p,h\right)|_{y=w_p}=\left(\bar{u},\bar{v},p,h\right)|_{y=0}. \tag{23}$$

The Maxwell stress, appearing as the last term on the right hand side of equation (21), is obtained via the solution of equation (7) for the electric potential; although equations (19)-(22) are valid for non-zero Re, their range of applicability is bounded by virtue of the long-wave limitation, namely to the case of small Capillary numbers only, that is $\mathrm{Ca}=\mu U_0/\sigma=\varepsilon^3/6\ll 1$. Note that, in contrast to the DAF used in Veremieiev et al (2010), equation (21) for the pressure is retained, rather than eliminating it as an unknown by substitution into equations (19) and (20); doing so minimises the computational time and effort associated with evaluating the Maxwell stress term.

Attention is restricted to film flows over simple step, trench and wavy bottom topographies. Since the topography profile appears as a function in the governing equations, completely sharp topographical features have to be approximated; accordingly, these are defined by arctangent functions (Stillwagon and Larson, 1988). For example, a rectangular trench is specified as follows:

$$\begin{aligned} s\left(x^*,y^*\right)=\frac{s_0}{4\tan^{-1}\left(\frac{l_t}{2\delta}\right)\tan^{-1}\left(\frac{w_t}{2\delta}\right)}&\left[\tan^{-1}\left(\frac{x^*+l_t/2}{\delta}\right)-\tan^{-1}\left(\frac{x^*-l_t/2}{\delta}\right)\right]\\ &\times\left[\tan^{-1}\left(\frac{y^*+w_t/2}{\delta}\right)-\tan^{-1}\left(\frac{y^*-w_t/2}{\delta}\right)\right], \end{aligned} \tag{24}$$

where $s_0(=S_0/H_0)$ is the non-dimensional depth ($s_0<0$), with $l_t(=L_t/L_0)$, $w_t(=(W_t/L_0)$ and δ defined as the non-dimensional streamwise length, spanwise width and steepness factor, respectively. The coordinate system $(x^*,y^*)=(x-x_t,y-y_t)$ has its origin at the centre of the topography (x_t,y_t). Note that for $\delta\ll 1$ the arctangent is a rapidly convergent function and thus topography defined according to equation (24) can be assumed to satisfy the periodic boundary conditions (17) to an acceptable degree of precision. Smoothly varying topography, such as a sinusoidal undulation, is easily specified via the appropriate functional form.

3 Method of solution

3.1 Hydrodynamic equations

Equations (19) to (22) are solved numerically, subject to the boundary conditions specified, on a rectangular computational domain, $(x,y)\in[0,l_p]\times[0,w_p]$, subdivided using a staggered

arrangement of unknowns. Taking $(i,j) \in [1,n_x] \times [1,n_y]$ to represent a typical mesh point in the system, where n_x and n_y are the total number of nodes, in the x and y directions, respectively, values of film thickness, h, and pressure, p, are located at (i,j), with averaged velocities $\bar{u}$ and $\bar{v}$ located at the mid-points $(i+1/2,j)$ and $(i,j+1/2)$, respectively; uniform spatial increments were employed, $\Delta x = l_p/n_x$ and $\Delta y = w_p/n_y$, such that $x_1 = 0$, $y_1 = 0$ and $x_{n_x} = l_p - \Delta x$, $y_{n_y} = w_p - \Delta y$. The use of such a staggered mesh arrangement avoids the well-known checkerboard instability that results if central differencing is applied to first-order pressure derivatives and to the terms in the continuity equation if the pressure and velocity components are collocated, Trottenberg, Oosterlee and Schüller (2001).

Writing discrete forms of the momentum equations (19) and (20) at $(i+1/2,j)$ and $(i,j+1/2)$, respectively and the pressure (21) and continuity (22) equations at (i,j), omitting for the sake of convenience the over-bar denoting averaged values, results in the following second-order accurate system of difference equations:

$$\frac{6}{5}\varepsilon \mathrm{Re} F\left[u\right]_{i+1/2,j} + \frac{p_{i+1,j} - p_{i,j}}{\Delta x} + \frac{3u_{i+1/2,j}}{h^2_{i+1/2,j}} - 2 = 0, \tag{25}$$

$$\frac{6}{5}\varepsilon \mathrm{Re} F\left[v\right]_{i,j+1/2} + \frac{p_{i,j+1} - p_{i,j}}{\Delta y} + \frac{3v_{i,j+1/2}}{h^2_{i,j+1/2}} = 0, \tag{26}$$

$$p_{i,j} + \frac{\varepsilon^3}{\mathrm{Ca}}\left(\frac{f_{i+1,j} + f_{i-1,j} - 2f_{i,j}}{\Delta x^2} + \frac{f_{i,j+1} + f_{i,j-1} - 2f_{i,j}}{\Delta y^2}\right) - 2\varepsilon \cot\theta f_{i,j} + \varepsilon \mathrm{We}\left(\frac{\partial \varphi}{\partial z}\right)^2 |_{z=f}|_{i,j} = 0, \tag{27}$$

$$\frac{h_{i+1/2,j}u_{i+1/2,j} - h_{i-1/2,j}u_{i-1/2,j}}{\Delta x} + \frac{h_{i,j+1/2}u_{i,j+1/2} - h_{i,j-1/2}u_{i,j-1/2}}{\Delta y} = 0, \tag{28}$$

where $F\left[\omega\right] = u\frac{\partial \omega}{\partial x} + v\frac{\partial \omega}{\partial y}$ is the convective operator, which is discretised using a first-order upwind scheme (Chung 2002); its value at the appropriate grid locations is obtained by interpolation between neighbouring nodes (Veremieiev et al 2010), as are the quantities $h_{i\pm1/2,j} = \left(h_{i\pm1,j} + h_{i,j}\right)/2$ and $h_{i,j\pm1/2} = \left(h_{i,j\pm1} + h_{i,j}\right)/2$. The evaluation of discrete values at (i,j) for the last quantity, the Maxwell stress term, on the right hand side of equation (27) is discussed subsequently.

The imposition of periodic boundary conditions requires the specification of ghost nodes at the edge of the computational domain in x and y directions, namely:

$$h_{i\pm n_x,j\pm n_y} = h_{i,j}, \quad p_{i\pm n_x,j\pm n_y} = p_{i,j}, \tag{29}$$

$$u_{i+1/2\pm n_x,j\pm n_y} = u_{i+1/2,j}, \quad v_{i\pm n_x,j+1/2\pm n_y} = v_{i,j+1/2}, \tag{30}$$

while, the Dirichlet condition for the film thickness at the inlet is assigned as an exact value there:

$$h|_{1,j} = 1. \tag{31}$$

In the particular case of a periodically repeating wavy substrate extending to the boundary the volume constraint condition, equation (14), is imposed, at the point $(i,j) = (1,1)$, by replacing equation (28) there by:

$$\sum_{i=1}^{n_x}\sum_{j=1}^{n_y} h_{i,j} = n_x n_y. \tag{32}$$

3.2 Electric field equation

An analytical solution to the three-dimensional Laplace problem (7), subject to boundary conditions (15)-(17) and the restriction $\varepsilon \ll 1$, is obtained as a Fourier series expansion using the method of separation of variables:

$$\varphi(x,y,z) = 1 - z + \frac{1}{l_p w_p} \int_0^{l_p} \int_0^{w_p} (f-1) \sum_{m,n=0}^{\infty} \chi_m \chi_n \cos\left[\lambda_m (x-\widehat{x})\right] \times \cos\left[\mu_n (y-\widehat{y})\right] \exp\left[-\left(\sqrt{\lambda_m^2+\mu_n^2}\right)\varepsilon z\right] d\widehat{x} d\widehat{y}, \tag{33}$$

the details of which are provided in Appendix A.

The z-derivative of the above potential, $\partial\varphi/\partial z|_{z=f}$, required to determine the vertical component of the electric field, is given by:

$$\frac{\partial \varphi}{\partial z}|_{z=f} = -1 - \varepsilon E\left[f-1\right](x,y), \tag{34}$$

where $E\left[f-1\right]$, is the electric field Fourier operator, namely:

$$E\left[f-1\right] \approx \frac{1}{l_p w_p} \int_0^{l_p} \int_0^{w_p} (f-1) \sum_{m,n=0}^{\infty} \chi_m \chi_n \sqrt{\lambda_m^2+\mu_n^2} \cos\left[\lambda_m (x-\widehat{x})\right] \cos\left[\mu_n (y-\widehat{y})\right] d\widehat{x} d\widehat{y}. \tag{35}$$

The Maxwell stress term, appearing on the right hand side of the pressure equation (21), is obtained by neglecting terms $\mathrm{O}(\varepsilon^3 \mathrm{We})$:

$$\varepsilon \mathrm{We} \left(\frac{\partial \varphi}{\partial z}\right)^2 |_{z=f} \approx \varepsilon \mathrm{We} + 2\varepsilon^2 \mathrm{We} E\left[f-1\right](x,y), \tag{36}$$

where the εWe term on the right hand side of equation (36) is a constant pressure term which can be omitted since the DAF equations are driven by the gradient of the pressure, not by the pressure itself.

The integrals associated with the E operator and hence the Maxwell stress term (36) which appears in equation (27), are evaluated numerically at the point (i,j) using trapezoidal quadrature, exploiting the periodicity of the solution, that is:

$$E\left[f-1\right]_{i,j} = \sum_{k=1}^{n_x} \sum_{l=1}^{n_y} E_{i,j,k,l} \left(f_{k,l} - 1\right), \tag{37}$$

with

$$E_{i,j,k,l} = \frac{1}{n_x n_y} \sum_{m,n=0}^{N^f} \chi_m \chi_n \sqrt{\lambda_m^2+\mu_n^2} \cos\left(\frac{2\pi m (i-k)}{n_x}\right) \cos\left(\frac{2\pi n (j-l)}{n_y}\right). \tag{38}$$

N^f is the number of terms in the truncated Fourier series.

3.3 Overall numerical procedure

The integro-differential electrohydrodynamic discrete equation set, (25)-(28), is solved using a numerical approach based on Newton iteration with generally up to ten of the latter required to reduce the residuals of the discrete equation set to a value below 10^{-6}. For two-dimensional flow over spanwise topography, the global Jacobian can be stored in memory and iteration

performed efficiently using the LU decomposition with partial pivoting via library routines readily accessible within LAPACK (Anderson et al, 1999). For the three-dimensional flows of interest, the global matrix generated is too large to be stored in memory; consequently an iterative matrix-free method of solution is required - in the present work the conjugate gradient normal residual (CGNR) method with Jacobi pre-conditioning was employed, full details of which are provided in Kelley (2003). The symmetric matrix required by the conjugate gradient solver is obtained by multiplying the iterative equations by the transpose of the Jacobian.

Symmetry ensures that only those $n_x \times n_y$ elements of $E_{i,j,k,l}$, equation (38), corresponding to all possible combinations of $|i-k|$ and $|j-l|$, need to be stored; even so evaluating the double summation for the operator E, equation (37), is computationally intensive. The effort required can be reduced considerably, without loss of accuracy, by neglecting to sum terms that lie far from the diagonals $i=k$ and $j=l$ (electric field tensors are strongly diagonally dominant and at the same time periodic) and far from the centre of the topography where the film approaches its asymptotic thickness. In which case, equation (37) for E can be rewritten as:

$$E\left[f-1\right]_{i,j} \approx \sum_{k,l\in\Omega} E_{i,j,k,l}\left(f_{k,l}-1\right), \tag{39}$$

where:

$$\begin{array}{c}\Omega = \left[i-\gamma n_x/2+1, i+\gamma n_x/2\right]\times\left[j-\gamma n_y/2+1, j+\gamma n_y/2\right] \\ \cup\left[i_t-\gamma n_x/2+1, i_t+\gamma n_x/2\right]\times\left[j_t-\gamma n_y/2+1, j_t+\gamma n_y/2\right],\end{array} \tag{40}$$

such that $(i_t, j_t) = (\mathrm{trunc}\left(x_t/\Delta x\right), \mathrm{trunc}\left(y_t/\Delta y\right))$ are the discretised coordinates of the centre of the topography; $\mathrm{trunc}\left(x\right)$ is the truncation function from real to integer. $\gamma \in [0,1]$ is an adjustable parameter that can be varied to ensure guaranteed solution accuracy at an acceptable computational cost; the values 1 and 0 correspond to integration over the whole or none of the solution domain, respectively.

Furthermore, in order to produce accurate solutions in an acceptable time, the CGNR method was parallelised using geometric domain decomposition, implemented via a message-passing interface (MPI) distributed memory paradigm, see Snir, Otto, Huss-Lederman, Walker and Dongarra (1996). For simplicity, strip-wise partitioning in the x-direction was used, ensuring that each subdomain has two immediate neighbours, including the first and the last subdomains due to the periodic nature of the solution. Each processor is responsible for the calculation of matrix-vector products for one subdomain only, which requires the use of additional columns of the solution immediately to either side of a subdomain; evaluating expression (39) over Ω results in the use of a significant number of additional columns.

In brief, on subdomain $i_p \in [0, n_p-1]$, where n_p is the total number of subdomains, the matrix-vector products are calculated for $i \in [i_1, i_2]$, with:

$$i_1 = \mathrm{loc}\cdot i_p + \min(i_p, \mathrm{rem}) + 1, i_2 = \begin{cases} (\mathrm{loc}+1)\cdot(i_p+1), & i_p < \mathrm{rem} \\ \mathrm{loc}\cdot(i_p+1)+\mathrm{rem}, & i_p \geq \mathrm{rem}\end{cases}, \tag{41}$$

where $\mathrm{loc} = \mathrm{trunc}\left(n_x/n_p\right)$ and $\mathrm{rem} = n_x - \mathrm{loc}\cdot n_p$, which requires the subdomains to overlap and to contain the solution for $i \in [i_3, i_4]$, where:

$$i_3 = \min(i_1, i_t) - \gamma n_x/2 + 1, \quad i_4 = \max(i_2, i_t) + \gamma n_x/2. \tag{42}$$

Point-to-point communication is used to exchange data between neighbouring subdomains, i.e. $i_p \rightarrow \left\{\begin{smallmatrix} i_p+1, i_p<n_p-1 \\ 0, i_p=n_p-1\end{smallmatrix}\right.$ and $i_p \rightarrow \left\{\begin{smallmatrix} i_p-1, i_p>0 \\ n_p-1, i_p=0\end{smallmatrix}\right.$, and one-to-all communication is used to exchange

data from subdomains that contain the neighbourhood of the centre of the topography to the remaining subdomains. Proceeding in this way requires the following restriction on the number of subdomains, namely $n_p \leq 2/\gamma$; one-to-all communication restricts the location of the centre of the topography so that its neighbourhood covers as small a number of subdomains as possible. For example, for $n_p = 2/\gamma$ the centre of the topography is desired to be $i_t = i_2$ so its neighborhood covers only two subdomains: i_p and $i_p + 1$. The amount of communication between subdomains is strictly dependant on the value of the summation parameter γ and has a large influence on the computational time. Acceptable parallel efficiency is achieved by setting $\gamma = 0.2$ and prescribing 8 subdomains; the computational time to convergence is reduced by a factor of between 6 and 7, compared to using a serial method, giving a parallel efficiency gain in excess of 75 %.

The number of operations required for the solution of the dense matrices arising from the discretisation of the integro-differential equation set concerned, using the specified solvers (serial LAPACK and 8 processor parallel CGNR), equate to approximately $O(N^3)$ and $O(N^{5/2})$ for the two-dimensional (spanwise topography) and three-dimensional (localised trench topography) problems of interest. In the former case, the CPU times involved are not large in terms of computing resource requirement and thus the number of nodes that can be employed is not a constraint, provided that sufficient are utilised to ensure mesh independence. Solving for the flow over a localised trench topography is a very much more demanding task in terms of CPU time. Without the latter being too overly prohibitive, even when using parallel processing, mesh independent solutions were generated by ensuring that the number of nodes employed in each coordinate direction was equal to the equivalent number required to guarantee mesh independent solutions in the case of the spanwise problems investigated, for the same range of flow parameters. A key enabler in this respect was to exploit the spanwise symmetry of the trench topography, by imposing symmetry boundary conditions at the mid-plane, $y^* = 0$.

4 Results

In the systematic investigation which follows, film flows with We up to and including cases where $\mathrm{We} = O(1/\varepsilon^2)$ are considered; the second term on the right hand side of equation (36) being significant. Although the system of the equations (19) - (22) contains five dimensionless parameters, ε, Re, Ca, We and θ, similarity considerations as well as the physics involved dictates a dependence on three dimensionless groupings only: an inertia $\mathcal{I} = \mathrm{Ca}^{1/3} \cdot \mathrm{Re}$ (Veremieiev et al, 2010), a gravity $\mathrm{N} = \mathrm{Ca}^{1/3} \cdot \cot\theta$ (Bertozzi and Brenner, 1997) and an electric field $\mathcal{W} = \mathrm{Ca}^{2/3} \cdot \mathrm{We}$ (Tseluiko et al, 2008a), parameter. Attention is focused initially on two-dimensional flows involving spanwise topography; this is followed by the first such exploration of the combined effects of both inertia and a normal electric field on three-dimensional film flow over localised topographical features.

The associated hydrodynamic stability limit of the flows of interest is important. As such, except where direct comparison is drawn with the work of others, the results presented adhere strictly to the classical linear stability constraint of a bounding critical Re_{crit}, as derived for film flow over a planar substrate (see, for example, Benjamin 1957 and Yih 1963), in terms of the inclination angle, namely:

$$\mathrm{Re}_{crit} = \frac{5}{4}\cot\theta; \tag{43}$$

giving, for the substrate inclination angles of $\theta = 2^\circ$ and 30° investigated subsequently corresponding Re_{crit} values of 35.8 and 2.17, respectively.

In addition, from the standpoint of electrified film flow, for the results obtained to be

physically and practically realisable, in all cases the size of E_0 has to be less than the critical value for the dielectric breakdown of air; this can be established for the problem of interest and an upper limit determined via Paschen's law, derived experimentally, see for example Meek and Craggs (1978) or Kuffel, Zaengl and Kuffel (2000):

$$V_B = A\sqrt{P_A D} + BP_A D, \quad E_B = A\sqrt{P_A/D} + BP_A, \tag{44}$$

where V_B, E_B, D and P_A is the breakdown potential difference between electrodes, the generated electric field strength, the distance between electrodes and the pressure of the gas concerned, respectively; A and B are dimensional constants characteristic of the gas. For thin water film (fluid properties $\rho = 1000\text{kg}\cdot\text{m}^{-3}$, $\mu = 0.001\text{Pa}\cdot\text{s}$ and $\sigma = 0.07\text{N}\cdot\text{m}^{-1}$), and taking $\theta = 30^\circ$ with $\varepsilon_e = 8.85\cdot 10^{-12}\text{F}\cdot\text{m}^{-1}$, typically $\varepsilon = 0.1$, $\text{Ca} = \varepsilon^3/6 = 0.000167$ and $\mathcal{W} = 3.0$, giving values for H_0 $\left[= \left(\frac{2\sigma \text{Ca}}{\rho G_0 \sin\theta}\right)^{1/2}\right]$ and E_0 $\left[= \left(\frac{\mathcal{W}}{\varepsilon_e}\right)^{1/2} (2\sigma\rho G_0 \sin\theta)^{1/4}\,\text{Ca}^{-1/12}\right]$ of $6.9\cdot 10^{-5}$ m and $6.2\cdot 10^6\text{V}\cdot\text{m}^{-1}$, respectively. Note, for tap water readily available in the laboratory, having an electrical conductivity typically $0.1\text{S}\cdot\text{m}^{-1}$ (Gray, 2008), the assumption that the same behaves as a perfectly conducting fluid is not infringed, Melcher and Taylor (1969).

For the above parameters, Figure 2 shows the dependencies V_B vs. $(P_A\cdot D)$ and E_B/P_A vs. $(P_A\cdot D)$ for air with $A = 6.76\cdot 10^4\text{V}\cdot(\text{atm}\cdot\text{m})^{-1/2}$ and $B = 2.47\cdot 10^6\text{V}\cdot(\text{atm}\cdot\text{m})^{-1}$ based on expressions (44), which provide an acceptable approximation over the range 10^{-5} to 10^0 $(\text{atm}\cdot\text{m})$. For a distance $D = 2\cdot 10^{-4}$m, which is greater than the film thicknesses $H_0 = 6.9\cdot 10^{-5}$m, and a pressure of $P_A = 1$atm an electric field strength of $E_B = 7.2\cdot 10^6\text{V}\cdot\text{m}^{-1}$ represents the dielectric breakdown limit which is greater than E_0. Moreover for pressures greater than atmospheric the breakdown electric field strength is even larger: for example, keeping $D = 2\cdot 10^{-4}$m, a value $P_A = 2$atm gives $E_B = 1.2\cdot 10^7\text{V}\cdot\text{m}^{-1}$.

4.1 Two-dimensional flow

An important distinction and advantage of the current model compared to the one used previously by Tseluiko and Blyth (2009) in their two-dimensional investigation of electrified film flows with inertia is that in their problem formulation the latter is accounted for within a standard lubrication model by the inclusion of an additional term of the form $\frac{\partial}{\partial x}\left(\frac{8}{15}\varepsilon \text{Re} h^6 \frac{\partial h}{\partial x}\right)$: first derived by Benney (1966) and obtained via a perturbation analysis and long-wave expansion of the unknowns of the problem on the basis that $\varepsilon \ll 1$, it has appeared many times subsequently in the context of thin films (Lin, 1974; Nakaya, 1975; Chang, 1986). This model, referred to here as lubrication with inertia (LUBI), in accounting for inertia does so only in terms of the first-order dynamics of the perturbation analysis, with the Reynolds number assumed strictly only $O(1)$. For two-dimensional flow the dimensionless steady-state LUBI model for the film thickness, h, scaled accordingly, is given by:

$$\frac{\partial}{\partial x}\left[\frac{2}{3}h^3 + \frac{8}{15}\varepsilon \text{Re} h^6 \frac{\partial h}{\partial x} - \frac{2}{3}\varepsilon \cot\theta h^3 \frac{\partial f}{\partial x} + \frac{\varepsilon^3}{3\text{Ca}} h^3 \frac{\partial^3 f}{\partial x^3} + \frac{1}{3}\varepsilon \text{We} h^3 \frac{\partial}{\partial x}\left(\frac{\partial \varphi}{\partial z}\right)^2 |_{z=f}\right] = 0. \tag{45}$$

In contrast the current formulation does not employ a perturbation analysis; it solves the leading terms to $O(1)$ and $O(\varepsilon)$ in a coupled way and as a result there is no $O(1)$ restriction on Re. For the degenerate case $\text{Re} = 0$ both models are equivalent.

The values of N^f, γ and n_x required to ensure accurate solutions independent of them is explored first, by considering gravity-driven, electrified film flow over a narrow, spanwise trench topography with $\theta = 2^\circ$, $\varepsilon = 0.1$, $\text{Re} = 30$, $\text{Ca} = \varepsilon^3/6 = 0.000167$, $l_t = 2$, $x_t = 50$, $|s_0| = 0.25$, $l_p = 100$ and $\delta = 0.001$. The free-surface disturbance generated for the case $\mathcal{W} = 1.5$ and

$\mathcal{W} = 3.0$ is obtained using the current hydrodynamic model with the Maxwell stress evaluated via both the Fourier solution of the Laplace problem and, for comparison purposes, a Hilbert form; note the latter, derived using complex variable theory (Tseluiko et al 2008a, 2008b), is applicable in two-dimensions only, giving:

$$\varepsilon \mathrm{We} \left(\frac{\partial \varphi}{\partial z} \right)^2 |_{z=f} \approx \varepsilon \mathrm{We} + 2\varepsilon^2 \mathrm{We} H \left[\frac{\partial f}{\partial x} \right] (x) \,, \tag{46}$$

c.f. equation (36), where H, the Hilbert transform operator, is defined as:

$$H\left[g\right](x) = \frac{1}{\pi} PV \int_{-\infty}^{\infty} \frac{g\left(\widehat{x}\right)}{x - \widehat{x}} d\widehat{x}, \tag{47}$$

with $g\left(x\right) = \partial f / \partial x$ and PV denoting the principal value of the integral. For periodic functions the Hilbert operator takes the particular form:

$$H\left[g\right](x) = \frac{1}{l_p} PV \int_{0}^{l_p} g\left(\widehat{x}\right) \cot \left[\frac{\pi \left(x - \widehat{x}\right)}{l_p} \right] d\widehat{x}. \tag{48}$$

In two-dimensions, the Fourier operator, $E\left[f-1\right]$, namely:

$$E\left[f-1\right](x) = \frac{1}{l_p} \int_{0}^{l_p} \left(f-1\right) \sum_{m=1}^{\infty} \chi_m \lambda_m \cos\left[\lambda_m \left(x - \widehat{x}\right)\right] d\widehat{x}, \tag{49}$$

and the Hilbert operator, $H\left[\partial f / \partial x\right]$, are equivalent; for completeness a proof of this is provided in Appendix B.

Figures 3(a) and 3(b) show the effect of N^f, when $\gamma = 0.2$ and $n_x = 1024$, on the predicted free-surface profile: $N^f = 200$ terms is sufficient to produce a solution, using the Fourier integral operator to evaluate the Maxwell stress, in excellent agreement with its Hilbert counterpart. Figures 3(c) and 3(d), on the other hand considers the effect of γ, confirming that with $N^f = 200$ terms and $n_x = 1024$ nodes a value of $\gamma = 0.2$ yields the same level of agreement, regardless of which approach is used to evaluate the Maxwell stress. Finally Figures 3(e) and 3(f), show that these same values of N^f, γ and $n_x = 1024$ are sufficient to guarantee mesh independent solutions for the parameter range of interest; they are indistinguishable from the same obtained on a mesh containing twice the number of nodes, that is $n_x = 2048$. The physical effect of increasing $\mathcal{W}$ from 0 to 1.5 is the formation of a sharper, larger capillary ridge and deeper free-surface depression accompanied by amplification of the small wavelength free-surface variations existing upstream of the trench; increasing $\mathcal{W}$ further to 3.0 suppresses the capillary ridge altogether.

Accordingly, all predictions presented henceforth were obtained with $N^f = 200$ and a sufficiently large value of γ: for the remaining two- and subsequent three-dimensional flow problems considered these were prescribed as $\gamma = 1.0$ and $\gamma = 0.2$, respectively; in each case, as in the above example, δ is set equal to 0.001, a value small enough to ensure solutions are effectively independent of it (Veremieiev et al, 2010).

Having established the credentials of the current model and the accuracy of the associated method of solution, predictions obtained with the same are compared with those obtained with the LUBI model; both of which are contrasted with corresponding finite element solutions of the full Navier-Stokes (N-S) equations and attendant boundary conditions, expressions (5), (6), (9) to (14) and (17), obtained in a manner similar to Scholle et al (2008a). The problem chosen for this purpose is that of electrified film flow, with $\varepsilon = 0.2$, $\mathrm{Ca} = \varepsilon^2 = 0.04$, $\theta = 30^\circ$, $n_x = 1024$, over a periodically wavy substrate given by $s\left(x^*\right) = s_0 \sin\left(2\pi x^* / l_p - \pi/2\right)$ with

amplitude $s_0 = 1.0$ and wavelength $l_p = 2\pi$, see Tseluiko and Blyth (2009). Flow in the absence of an electric field ($\mathcal{W} = 0$) are considered in Figures 4(a) & (b), showing that: (i) all three solutions are indistinguishable when Re = 0; (ii) while the DAF and N-S solutions remain indistinguishable, for the case Re = 10, there is a clear discrepancy in terms of the predicted free-surface shape between them and LUBI solution. The reason for the excellent agreement between the DAF and N-S solutions can be explained with reference to Figures 4(c) & (d): in both cases the steamline plots reveal the unidirectional nature of the flow, thus establishing the appropriateness of the assumed classical Nusselt like velocity profile underpinning the DAF model. The flow structure present also agrees with the findings of Scholle et al (2008a), who predicted that no eddy, inertial or kinematic, is present when the thin film parameter as defined there in is $2\pi\varepsilon/l_p = 0.2 \ll 1$. The discrepancy for Re = 10 shown by the LUBI solution is attributable to the fact that for this model, Re must be strictly O(1) or smaller. Finally, Figures 4 (e) & (f) compare the free-surface profiles obtained with the DAF and the LUBI models for electrified film flow with $\mathcal{W} = 2.92$; once again, although the solutions obtained with the two different approaches are indistinguishable for Re = 0, a discrepancy between the two emerges for Re > 0 for the reason discussed above.

For the above problem the topography is smoothly varying; disagreement between LUBI solutions and their DAF and N-S counterparts becomes further exacerbated when the topography concerned is steep, yet satisfying the long-wave constraint. This is demonstrated in Figure 5 which provides a comparison of the the free-surface disturbance predicted by the DAF, LUBI and N-S models for the same narrow spanwise trench problem used to generate Figure 3; $\theta = 2^\circ$, $\varepsilon = 0.1$, Re $= 0, 10, 30$, Ca $= \varepsilon^3/6 = 0.000167$, $l_t = 2$, $x_t = 50$, $|s_0| = 0.25$, $l_p = 100$ and $\mathcal{W} = 0, 1.5$. When Re = 0, Figures 5 (a) & (b) reveal, as anticipated, excellent agreement. Increasing the the electric field strength, that is $\mathcal{W}$, from 0 to 1.5 has a pronounced effect on the resulting free-surface shape; a more detailed discussion of which is left till later. For $\mathcal{W} = 0$ and non-zero Re, Figures 5 (c) & (e), the expected discrepancy between the LUBI and the DAF and N-S solutions is clearly seen, especially when Re = 30, the latter two being indistinguishable. Figures 5 (d) & (f) show the same features occurring but this time for the case $\mathcal{W} = 1.5$; of particular note is the predicted over-amplification of the upstream oscillatory behaviour of the free-surface associated with the LUBI solution.

Continuing with the theme of steep topography, the next problem explored is that of electrified film flow on an inclined plane containing step-down and step-up topography forming the sides of a wide spanwise trench; as in the case of of the narrow trench explored above, it represents a natural and important precursor to the three-dimensional flows investigated subsequently. It is the same problem as considered by Tseluiko et al (2008a) for the one case Re = 0 and $\theta = 90^\circ$, with $\varepsilon = 0.1$, Ca $= \varepsilon^3 = 0.001$. The topography used in their analysis ($|s_0| = 2.0$) lies outside the bounds for which the long-wave approximation can be considered as strictly valid (Gaskell et al, 2004). Note also that, the step-up solutions they report are in error; the same having been established following correspondence with and further calculations by the authors (Blyth, 2010); the correct solution is provided in Veremieiev (2011). In the present work a more representative smaller step height is employed and the investigation extended to the case Re > 0 ($\theta = 2^\circ$, $\varepsilon = 0.1$ and Ca $= \varepsilon^3/6 = 0.000167$, $|s_0| = 0.25$, with $l_t = 80$, $l_p = 200$, $x_t = 120$, $n_x = 2048$).

For the step-down cases, Figures 6(a) and 6(b), increasing Re from 0 to 30 when $\mathcal{W} = 0$ leads to an increase in the size of the capillary ridge, while increasing the electric field strength, for both Re = 0 and 30, has a much more dramatic effect on the overall free-surface profile. Increasing $\mathcal{W}$ to 1.5 leads to a downstream displacement and narrowing of the capillary ridge and to a broad free-surface trough just upstream of the step. Increasing $\mathcal{W}$ further to 3.0 is sufficient to completely suppress the capillary ridge; this is accompanied by a deepening of

the free-surface trough. For the step-up cases, Figures 6(c) and 6(d), increasing Re to 30 in the absence of an electric field results in a slightly deeper free-surface trough, just upstream of the step, while increasing $\mathcal{W}$ to 1.5 leads to a downstream displacement toward the step and a narrowing of this trough together with the formation of a free-surface hump. Unlike the capillary ridge at a step-down, increasing $\mathcal{W}$ to 3.0 leads to further enhancement of the free-surface hump accompanied by a further downstream displacement. Shown also, for comparison purposes, Figures 6(e) and 6(f), are the results obtained for the flow over the same narrow trench topography as discussed above. They show that the flow is only marginally affected by increasing inertia in the absence of an electric field, resulting in a slight enhancement of both the capillary ridge and free-surface depression. As in the step cases, the free-surface disturbance experienced it is much more sensitive to the value of $\mathcal{W}$: increasing $\mathcal{W}$ from 0 to 1.5 leads to significant amplification of the capillary ridge and free-surface depression together with the formation of a downstream hump, while increasing $\mathcal{W}$ further to 3.0 gives rise to almost complete suppression of the capillary ridge, a diminution of the free-surface depression and amplification of the hump.

For both topographic features, the narrow and wide trench, simultaneous amplification occurs of the small wavelength free-surface disturbances lying upstream, which are present even when $\mathcal{W} = 0$; the nature of this oscillatory behaviour, observed also in Figure 3, is a function of the competition between the geometry (topography height and steepness) producing the free-surface curvature and capillary pressure tending to oppose it, see for example Kalliadasis, Bielarz and Homsy (2000) and the experimental work of Stillwagon and Larson (1988, 1990). A similar feature is observed in the three-dimensional thin film flows explored subsequently.

The results of a corresponding extensive parameter study into the effects of non-zero Re and $\mathcal{W}$ on the free-surface profiles associated with the step-up and step-down sides of the wide trench problems considered in Figures 6 (a) to (d), are summarised in Figure 7. Figure 7(a) shows that for the step-down case, for a fixed Re, the predicted maximum value of the capillary ridge increases monotonically with increasing $\mathcal{W}$, peaking before diminishing more rapidly, again monotonically. This result shows also, that the larger the value of Re the larger the value of $\mathcal{W}$ required to suppress the inertially-enhanced free-surface disturbances. For example, complete suppression of the capillary ridge (corresponding to a maximum value $f = 1$) for Re = 0, 30 and 50 is achieved by values of $\mathcal{W} \approx 2.25$, 2.35 and 2.45, respectively. In the case of a step-up, Figure 7(b), the maximum value corresponds to that for the free-surface hump that appears which is found to increase monotonically with increasing $\mathcal{W}$. However, in contrast to the step-down case, the maximum value remains more or less unaffected by the value of the Re for values of $\mathcal{W}$ less than approximately 1.75; beyond which point the curves diverge while continuing to increase monotonically before plateauing off. In the step-up case, increasing inertia acts to reduce the size of the electric-field induced free-surface amplification beyond $\mathcal{W} \approx 1.75$; while in the step-down case, increasing inertia increases the amplification of the capillary ridge for all values of $\mathcal{W}$ up until the point of complete suppression.

Note that Figure 7 contains results for Re = 50, a value which is strictly outside of the critical Re limit of 35.8 sanctioned by equation (43). Nevertheless, the rationale for including it is that in the experiments of Decré and Baret (2003) they were able to achieve stable flows for thin films on a substrate inclined at $\theta = 30^\circ$ to the horizontal and containing topographical features of the same dimensions, at a Re value of 3.54, one significantly larger than the critical limit of 2.17 by a factor of 1.63. Being conscious of the fact that experiments are prone to measurement errors, while noting as discussed in the Introduction that topography has been reported to increase the critical Re beyond which thin films become unstable, applying the same scaling factor for the case of film flow on a substrate inclined at $\theta = 2^\circ$ to the horizontal results in a critical Re limit of 58.3. Although a speculative result recognising that an applied

electric field can have an opposite, de-stablising effect, it is non-the-less complementary. In their work, Tseluiko et al (2008a) reported, for the case Re = 0, that while the maximum value of the free-surface hump formed at a step-up by the presence of an electric field increased monotonically with increasing $\mathcal{W}$, the maximum value of the free-surface at the capillary ridge formed at a step-down decreased monotonically from its largest value at $\mathcal{W} = 0$ with increasing $\mathcal{W}$. The difference in behaviour associated with the step-down to that observed in the present work, is a consequence of their choice of $|s_0| > 1.0$

Figure 8 considers the effect of $\mathcal{W}$ on the various stress contributions to the fluid pressure for zero Reynolds number flow over the narrow trench topography considered in Figures 6(e) & (f), for a substrate inclination angle, θ, of 30°. Since the hydrostatic pressure is only O(ε) in this case, the free-surface profile for $\mathcal{W} > 0$ is dominated by the competition between the O(1) capillary and Maxwell stress terms. For $\mathcal{W} = 1.5$, the large negative Maxwell stress just upstream of the trench requires a compensating large, positive capillary pressure which acts so as to enhance the capillary ridge. Similarly, the large positive Maxwell stress peak over the trench requires a large negative capillary pressure which enhances the size of the free-surface trough. For $\mathcal{W} = 3.0$, the significantly reduced Maxwell stresses upstream of the topography require much smaller capillary pressures (smaller even than for the $\mathcal{W} = 0$ case) leading to an effective suppression of the capillary ridge.

4.2 Three-dimensional flow

Turning now to the more practically relevant case of three-dimensional film flow, use is made of the electrohydrodynamic formulation of Section 2 to investigate a series of problems associated with the flow of a thin electrified water film over a localised trench topography. The substrate, $l_p = w_p = 100$, containing the trench, aspect ratio $A = w_t/l_t$, $l_t = 2$, $|s_0| = 0.25$ centred at $x_t = y_t = 50$, is inclined at $\theta = 30°$ to the horizontal ($\varepsilon = 0.1$, Ca $= \varepsilon^3/6 = 0.000167$ and exploiting symmetry $n_x = 1024$, $n_y = 512$).

Figures 9 and 10 analyse the effect of $\mathcal{W}$ on the transition of the flow from a three- to an essentially two-dimensional one through the centre of the topography in the steamwise direction, as the trench aspect ratio $A = w_t/l_t$ is increased. Figure 9(a)-(f) show the free-surface disturbance that is generated for the cases A = 5 and 10 when $\mathcal{W} = 0$, 1.5 and 3.0. As reported in Gaskell et al (2004), for $\mathcal{W} = 0$ as shown in Figures 10(a) and 10(b), decreasing A leads to a much reduced upstream capillary ridge and the formation of a small downstream surge caused by liquid entering the sides of the trench. Increasing $\mathcal{W}$ to 1.5 leads to a significant amplification of both the capillary ridge, just upstream of the trench, and the free-surface depression over the trench. This is accompanied by the disappearance of the downstream surge for $A = 1$. Increasing $\mathcal{W}$ further to 3.0 causes a general diminution in the magnitude of the free-surface disturbances; this is seen most clearly by the free-surface profiles given in Figures 10(e) and 10(f). Shown for comparison purposes on each of the plots is the free-surface disturbance for infinite A, that is an equivalent spanwise trench.

Figure 11 shows the effect of gradually increasing $\mathcal{W}$, for Re = 0, in steps of 0.5 from 0 to 3.5, on the free-surface disturbances generated by flow over a square trench topography, $A = 1$. It reveals that increasing $\mathcal{W}$ from 0 to 0.5 causes the horseshoe-shaped disturbance typical of such flows to broaden in the spanwise direction, accompanied by enhancement of the upstream capillary ridge and a diminution of the downstream surge. As in the two-dimensional spanwise trench case, Figure 6(e), increasing $\mathcal{W}$ beyond 0.5 leads to a significant amplification of both the free-surface peak and trough. This is seen particularly clearly for $\mathcal{W} = 1.5$, where the maximum non-dimensional height of the free surface increases from 1.01 (for $\mathcal{W} = 0$) to 1.08 and the minimum free-surface height decreases from 0.89 to 0.86. For $\mathcal{W} \geq 1$ the familiar

comet tail and bow-wave disturbances have all but disappeared. In contrast, increasing $\mathcal{W}$ from 1.0 to 2.0 causes the upstream capillary ridge to grow in magnitude and at $\mathcal{W} \approx 1.5$ a second capillary ridge is formed upstream of the first one. Beyond $\mathcal{W} = 1.5$ the magnitude of the primary free-surface peaks and troughs are reduced and become more sharply focussed. For $\mathcal{W} = 3.5$ the free-surface disturbances have been effectively planarised with maximum and minimum non-dimensional free-surface heights of just 1.02 and 1.05, respectively. The effect of $\mathcal{W}$ on the magnitude of the free-surface disturbances are shown more clearly by the streamwise and spanwise free-surface profiles shown in Figure 12.

Next the same sequence of events is considered but this time for the case of significant inertia, by taking $\theta = 2^\circ$. The cases shown in Figures 13 and 14 can be compared qualitatively with their counterparts shown in Figures 11 and 12 for which $\mathrm{Re} = 0$ and $\theta = 30^\circ$. Clearly, increasing $\mathcal{W}$ has a much larger influence than increasing Re and these are shown more clearly via the corresponding streamwise and spanwise free-surface profiles through the centre of the topography. In essence, increasing inertia when the value of $\mathcal{W}$ is fixed simply results in a slightly greater minimum streamwise depression across the trench that is shifted upstream. As noted in the section on two-dimensional flows, free-surface disturbances in electrified films arise due to the competition between the capillary and Maxwell stresses that act in opposition to each other.

Figure 15 illustrates the distribution of the capillary pressure and Maxwell stress in three-dimensional flow via contour plots for the $\mathcal{W} = 0$, 1.5 and 3.0 cases considered in Figures 11 and 12. In the absence of Maxwell stresses, $\mathcal{W} = 0$, the regions of negative and positive capillary pressure upstream and downstream of the trench topography, respectively, result in the capillary ridge and downstream surge. Increasing $\mathcal{W}$ to 1.5, leads to larger regions of significant positive and negative capillary pressure that are opposed by the development of larger regions of significant Maxwell stress. The larger values of negative capillary pressure, in particular, result in the large free-surface peak seen in Figure 11(d) while the large positive capillary pressures give rise to a larger free-surface depression over the topography. The competition between the capillary and Maxwell stresses are seen more clearly in the free-surface profiles given in Figure 16. This shows, in particular, how the capillary and Maxwell stresses effectively cancel each other out at higher $\mathcal{W}$ values, resulting in the planarised free-surface profiles shown in Figures 11 and 12.

5 Conclusions

Two- and three-dimensional electrified, continuous gravity-driven thin film flow over topography at finite Reynolds numbers has been explored by the novel coupling of a depth-averaged formulation of the Navier-Stokes equations with a general Fourier series solution of Laplace's equation for the electric field potential. For two-dimensional flow, the spanwise topography investigated include discrete step-up and step-down features and a narrow trench comprised of the same in close proximity, together with flow over a smooth periodically varying substrate; localised trench topography only is considered in the case of three-dimensional flow.

The detailed investigation carried out with regard to two-dimensional flow reveals a number of important new results, both from a theoretical and physical standpoint. Among these is the importance of the choice of hydrodynamic model if Reynolds number effects are to be captured satisfactorily and the same applied in a region of parameter space for which it is valid. That the current model is superior to a lubrication one, containing an additional term to account for inertia, is amply demonstrated; in particular with reference to corresponding finite element solutions for film flow over both spanwise smooth sinusoidally varying and trench topography.

A key outcome concerns the predicted free-surface response to increasing electric field strength for the case of film flow over spanwise step-down and step-up topography, the same being the constituent parts of a wide trench. For the non-zero Reynolds number values explored, at a step-down as the electric field strength is increased the free-surface maximum disturbance first increases monotonically, reaches a peak and then decreases monotonically to reach a point where the characteristic capillary ridge is completely suppressed. At a step-up the downstream hump which forms as the electric field strength is increased constitutes the maximum free-surface disturbance and which continues to increase monotonically; the larger the value of the Reynolds number the smaller the increase achieved.

As to the more practically relevant three-dimensional flow problems considered, increasing inertia generally enhances the magnitude of the capillary ridge that forms upstream of localised trench topography and reduces the magnitude of the free-surface surge as fluid exits the trench region. However, for the parameter range considered, the inclusion of an electric field dominates inertial effects so that inertially-induced disturbances can generally be suppressed by increasing the electric field strength. The electrified thin film flow over the trench topography cases considered clearly demonstrate that although the introduction of an electric field initially amplifies the size of the free-surface disturbances in the neighbourhood of the trench, increasing its strength eventually suppresses the persistent bow-wave disturbances that arise, leading to a more planarised film surface. In addition, for higher electric field strengths the pressure inside of the trench is raised restricting flow into it as the film passes over, thus reducing the amount of the fluid emerging from the trench at its downstream side and consequently the size of the downstream surge. The corresponding variations in the balancing capillary pressure explain the initial enhancement and then suppression of free-surface disturbances as Weber number increases. Maxwell stress depends not only on the value of the Weber number but also on the degree of the free-surface disturbance; for higher Weber number values the free surface becomes more planar, the Maxwell stresses diminish, which as a consequence reduces the capillary pressure and so on.

With regard to the issue of product quality, it is found that for flow over both steep spanwise and localised topography, regardless of whether or not inertia is present, while an electric field can be used to suppress the principal gross free-surface disturbances toward planarity, large values exacerbate the underlying oscillatory behaviour that arises as a consequence of the competition between the underlying geometry (topography height and steepness) giving rise to free-surface curvature and surface tension tending to oppose it. The observed behaviour is reminiscent of the ribbing instability that arises in the nip region of a forward roll coater, in that beyond a critical roll speed ratio additional free-surface curvature is created in the form of ribs to increase capillary pressure and maintain pressure equilibrium at the liquid-air interface, Weinstein and Ruschak (2004). The general observation is that when an electric field is present, the resultant free-surface disturbance is a consequence of the competition between the dominant capillary pressure and Maxwell stresses generated, with hydrostatic pressure having only a minor influence.

Acknowledgements

SV gratefully acknowledges the financial support of the European Union Marie Curie Action, contract MEST-CT-2005-020599.

Appendix A

The three-dimensional boundary value problem (7) for the electric field, together with boundary conditions (15) - (17), is solved by the method of separation of variables together with the same expanded as a Fourier series.

First the problem is made more tractable, see Tseluiko et al (2008a), by: (i) defining a *shifted* electric field potential, $\tilde{\varphi} = \varphi - 1 + z$, measuring the deviation from a uniform electric field; (ii) rescaling the z-coordinate with respect to ε such that $\tilde{z} = \varepsilon z$. Then with $(x, y, \tilde{z}) = (X, Y, Z)/L_0$ and $\nabla = \left(\frac{\partial}{\partial x}, \frac{\partial}{\partial y}, \frac{\partial}{\partial \tilde{z}}\right)$, the equivalent boundary value problem for $\tilde{\varphi}(x, y, \tilde{z})$ is

$$\nabla^2 \tilde{\varphi} = 0, \tag{50}$$

subject to the boundary conditions:

$$\tilde{\varphi}|_{\tilde{z}=\varepsilon f} = f - 1, \tag{51}$$

$$\nabla \tilde{\varphi}|_{\tilde{z}\to\infty} = 0, \tag{52}$$

$$\tilde{\varphi}|_{x=l_p} = \tilde{\varphi}|_{x=0}, \quad \tilde{\varphi}|_{y=w_p} = \tilde{\varphi}|_{y=0}. \tag{53}$$

Under the over arching assumption that $\varepsilon \ll 1$ the free-surface boundary condition (51) can be approximated as

$$\tilde{\varphi}|_{\tilde{z}=0} = f - 1. \tag{54}$$

Now, postulating the solution to have a separable form

$$\tilde{\varphi} = A(x)\, B(y)\, C(\tilde{z}), \tag{55}$$

substituting it into equation (50) and dividing through by $\tilde{\varphi}$ leads to the following equation for the separable components:

$$\frac{1}{A}\frac{d^2A}{dx^2} + \frac{1}{B}\frac{d^2B}{dy^2} + \frac{1}{C}\frac{d^2C}{d\tilde{z}^2} = 0, \tag{56}$$

which is satisfied via solutions of the following eigenvalue problems:

$$\frac{d^2A}{dx^2} + \lambda^2 A = 0, \quad \frac{d^2B}{dy^2} + \mu^2 B = 0, \quad \frac{d^2C}{d\tilde{z}^2} - \left(\lambda^2 + \mu^2\right) C = 0, \tag{57}$$

where λ and μ are real constants. Solving equations (57) subject to boundary conditions (52) and (53) leads to the following eigenvalues and eigenfunctions:

$$\lambda_m = 2\pi m / l_p, \quad A_m(x) = c_{1,m} \cos(\lambda_m x) + c_{2,m} \sin(\lambda_m x),$$

$$\mu_n = 2\pi n / w_p, \quad B_n(y) = c_{3,n} \cos(\mu_n y) + c_{4,n} \sin(\mu_n y),$$

$$C_{m,n}(\tilde{z}) = c_{5,m,n} \exp\left[-\left(\sqrt{\lambda_m^2 + \mu_n^2}\right)\tilde{z}\right], \quad \text{for } m = 0, 1...\infty, n = 0, 1...\infty, \tag{58}$$

which in turn results in a shifted potential of the form:

$$\tilde{\varphi}(x, y, \tilde{z}) = \sum_{m,n=0}^{\infty} [a_{m,n} \cos(\lambda_m x) \cos(\mu_n y) + b_{m,n} \sin(\lambda_m x) \sin(\mu_n y)$$

$$+ c_{m,n} \cos(\lambda_m x) \sin(\mu_n y) + d_{m,n} \sin(\lambda_m x) \cos(\mu_n y)] \exp\left[-\left(\sqrt{\lambda_m^2 + \mu_n^2}\right)\tilde{z}\right] \tag{59}$$

where $a_{m,n} = c_{5,m,n}c_{1,m}c_{3,n}$, $b_{m,n} = c_{5,m,n}c_{2,m}c_{4,n}$, $c_{m,n} = c_{5,m,n}c_{1,m}c_{4,n}$ and $d_{m,n} = c_{5,m,n}c_{2,m}c_{3,n}$ are arbitrary constants. From the free-surface boundary condition (54) it follows that these coefficients are the two-dimensional Fourier series expansion coefficients of $(f-1)$:

$$a_{m,n} = \frac{\chi_m \chi_n}{l_p w_p} \int_0^{l_p} \int_0^{w_p} (f-1) \cos(\lambda_m \widehat{x}) \cos(\mu_n \widehat{y})\, d\widehat{x} d\widehat{y}, \tag{60}$$

$$b_{m,n} = \frac{\chi_m \chi_n}{l_p w_p} \int_0^{l_p} \int_0^{w_p} (f-1) \sin(\lambda_m \widehat{x}) \sin(\mu_n \widehat{y})\, d\widehat{x} d\widehat{y}, \tag{61}$$

$$c_{m,n} = \frac{\chi_m \chi_n}{l_p w_p} \int_0^{l_p} \int_0^{w_p} (f-1) \cos(\lambda_m \widehat{x}) \sin(\mu_n \widehat{y})\, d\widehat{x} d\widehat{y}, \tag{62}$$

$$d_{m,n} = \frac{\chi_m \chi_n}{l_p w_p} \int_0^{l_p} \int_0^{w_p} (f-1) \sin(\lambda_m \widehat{x}) \cos(\mu_n \widehat{y})\, d\widehat{x} d\widehat{y}, \tag{63}$$

$$\chi_m = \begin{cases} 1, & \text{if} \quad m = 0 \\ 2, & \text{if} \quad m > 0 \end{cases}. \tag{64}$$

Since $\cos(\lambda_m x)\cos(\lambda_m \widehat{x}) + \sin(\lambda_m x)\sin(\lambda_m \widehat{x}) = \cos[\lambda_m (x - \widehat{x})]$ equation (59) can be expressed as follows:

$$\tilde{\varphi}(x, y, \tilde{z}) = \frac{1}{l_p w_p} \int_0^{l_p} \int_0^{w_p} (f-1) \sum_{m,n=0}^{\infty} \chi_m \chi_n \cos[\lambda_m (x - \widehat{x})]$$

$$\times \cos[\mu_n (y - \widehat{y})] \exp\left[-\left(\sqrt{\lambda_m^2 + \mu_n^2}\right) \tilde{z}\right] d\widehat{x} d\widehat{y}. \tag{65}$$

The potential is obtained by returning from the *rescaled* vertical coordinate $\tilde{z}$ to z and then from the *shifted* to the initial form of the electric potential:

$$\varphi(x, y, z) = 1 - z + \frac{1}{l_p w_p} \int_0^{l_p} \int_0^{w_p} (f-1) \sum_{m,n=0}^{\infty} \chi_m \chi_n \cos[\lambda_m (x - \widehat{x})]$$

$$\times \cos[\mu_n (y - \widehat{y})] \exp\left[-\left(\sqrt{\lambda_m^2 + \mu_n^2}\right) \varepsilon z\right] d\widehat{x} d\widehat{y}. \tag{66}$$

Appendix B

Proof of the equivalence of the Hilbert operator, $H[\partial f/\partial x]$, and two-dimensional Fourier operator, $E[f-1]$, for the Maxwell stress.

Use is made of the following two expressions:

1. The Fourier expansions of $(f-1)$ and $\partial f/\partial x$:

$$f(x) - 1 = \sum_{m=0}^{\infty} [a_m \cos(\lambda_m x) + b_m \sin(\lambda_m x)], \tag{67}$$

$$\frac{\partial f}{\partial x} = \sum_{m=1}^{\infty} \lambda_m [-a_m \sin(\lambda_m x) + b_m \cos(\lambda_m x)], \tag{68}$$

where

$$a_m = \frac{\chi_m}{l_p} \int_0^{l_p} (f-1) \cos(\lambda_m \widehat{x})\, d\widehat{x}, \quad b_m = \frac{\chi_m}{l_p} \int_0^{l_p} (f-1) \sin(\lambda_m \widehat{x})\, d\widehat{x}. \tag{69}$$

2. The Principal Values (PV) of integrals for positive number $\lambda_m > 0$:

$$PV\int_{-\infty}^{\infty}\frac{\sin\left[\lambda_m\left(x-\widehat{x}\right)\right]}{\widehat{x}}d\widehat{x}=\sin\left(\lambda_m x\right)PV\int_{-\infty}^{\infty}\frac{\cos\left(\lambda_m\widehat{x}\right)}{\widehat{x}}d\widehat{x}$$
$$-\cos\left(\lambda_m x\right)PV\int_{-\infty}^{\infty}\frac{\sin\left(\lambda_m\widehat{x}\right)}{\widehat{x}}d\widehat{x}=-\pi\cos\left(\lambda_m x\right), \tag{70}$$

$$PV\int_{-\infty}^{\infty}\frac{\cos\left[\lambda_m\left(x-\widehat{x}\right)\right]}{\widehat{x}}d\widehat{x}=\cos\left(\lambda_m x\right)PV\int_{-\infty}^{\infty}\frac{\cos\left(\lambda_m\widehat{x}\right)}{\widehat{x}}d\widehat{x}$$
$$+\sin\left(\lambda_m x\right)PV\int_{-\infty}^{\infty}\frac{\sin\left(\lambda_m\widehat{x}\right)}{\widehat{x}}d\widehat{x}=\pi\sin\left(\lambda_m x\right), \tag{71}$$

where Dirichlet integration has been used.

Starting with the Hilbert operator (47), inserting into it the Fourier representation (68) and taking into account the PV integrals (70) and (71) gives:

$$H\left[\frac{\partial f}{\partial x}\right](x)=\frac{1}{\pi}PV\int_{-\infty}^{\infty}\frac{\partial f\left(\widehat{x}\right)}{\partial\widehat{x}}\frac{d\widehat{x}}{x-\widehat{x}}=\frac{1}{\pi}PV\int_{-\infty}^{\infty}\frac{\partial f\left(x-\widehat{x}\right)}{\partial\widehat{x}}\frac{d\widehat{x}}{\widehat{x}}$$
$$=\frac{1}{\pi}\sum_{m=1}^{\infty}\lambda_m PV\int_{-\infty}^{\infty}\left\{-a_m\frac{\sin\left[\lambda_m\left(x-\widehat{x}\right)\right]}{\widehat{x}}+b_m\frac{\cos\left[\lambda_m\left(x-\widehat{x}\right)\right]}{\widehat{x}}\right\}d\widehat{x}$$
$$=\sum_{m=1}^{\infty}\lambda_m\left[a_m\cos\left(\lambda_m x\right)+b_m\sin\left(\lambda_m x\right)\right]$$
$$=\frac{1}{l_p}\int_0^{l_p}\left(f-1\right)\sum_{m=1}^{\infty}\chi_m\lambda_m\cos\left[\lambda_m\left(x-\widehat{x}\right)\right]d\widehat{x}=E\left[f-1\right](x), \tag{72}$$

which is the two-dimensional Fourier operator (49).

Figures

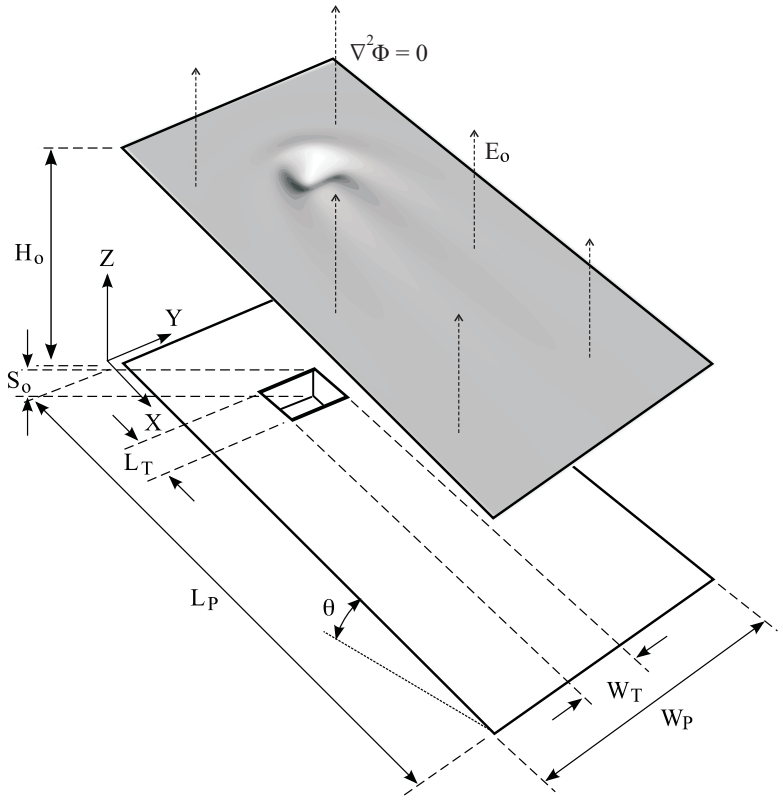

Figure 1: Schematic of gravity-driven three-dimensional flow over a substrate containing a trench topography in the presence of a uniform electric field applied normal to the substrate.

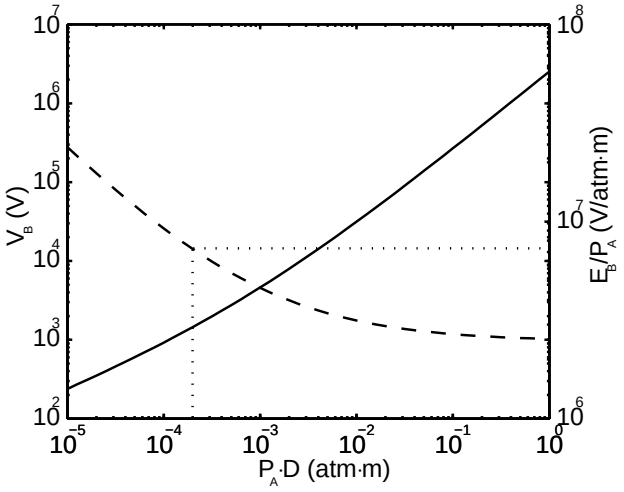

Figure 2: Plot of V_B (full line) and E_B/P_A (dashed line) against $P_A \cdot D$, for the dielectric breakdown of air. The point at which $D = 2 \cdot 10^{-4}$ m, $P_A = 1$ atm and $E_B = 7.2 \cdot 10^6 \mathrm{V} \cdot \mathrm{m}^{-1}$ is denoted by the dotted lines.

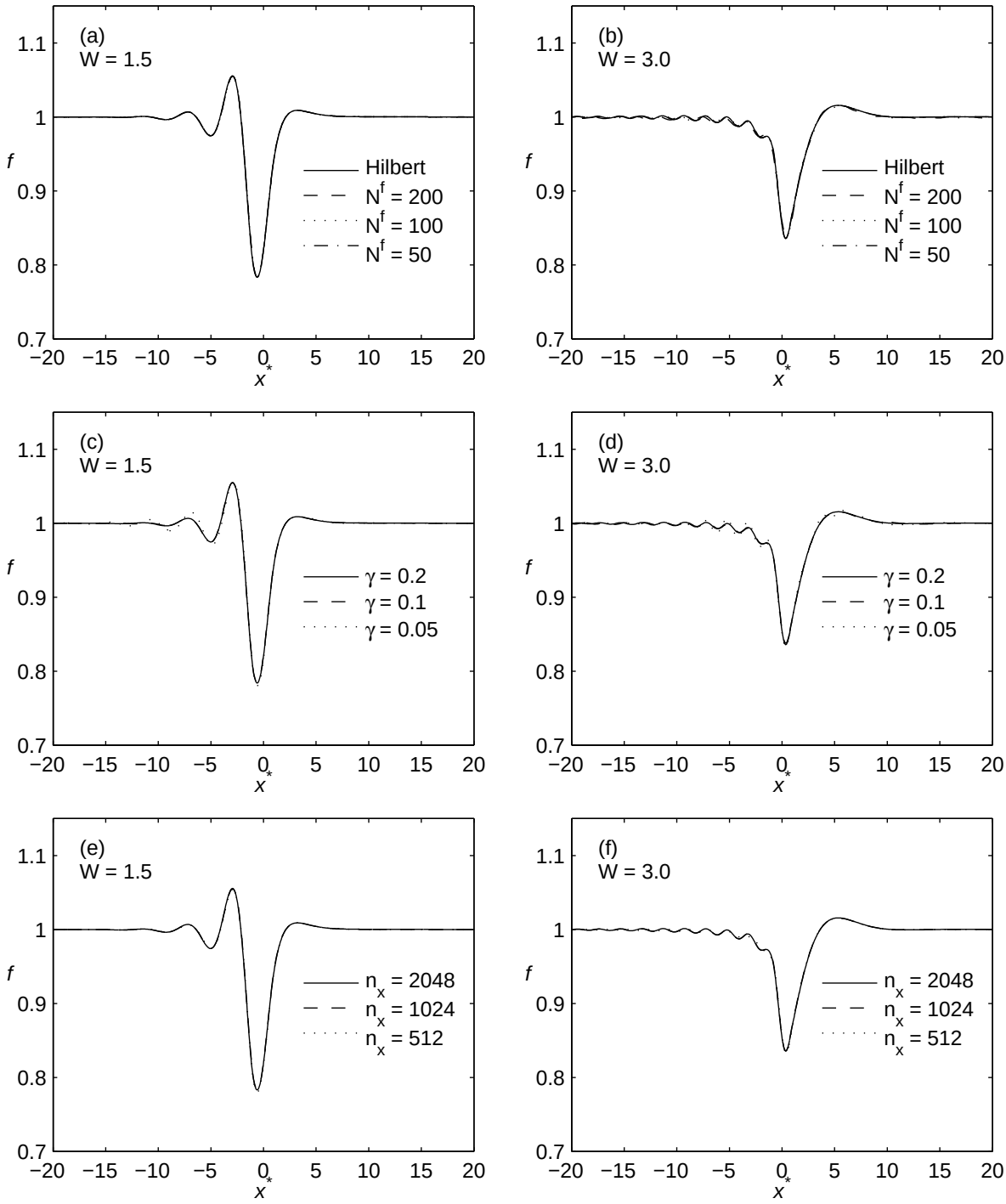

Figure 3: The effect of the value of N^f for $\gamma = 0.2$ and $n_x = 1024$ (top), γ for $N^f = 200$ and $n_x = 1024$ (middle) and n_x for $\gamma = 0.2$ and $N^f = 200$ (bottom) on DAF predicted free-surface profiles for thin film flow over a spanwise narrow trench topography ($\theta = 2°$, Re = 30, $l_t = 2$, $|s_0| = 0.25$), see Figure 5; $\mathcal{W} = 1.5$ (left) and $\mathcal{W} = 3.0$ (right). The corresponding results obtained with the Hilbert integral operator (48) are included in (a) and (b) for comparison purposes; these are found to be in excellent agreement with and indistinguishable from the results obtained with the Fourier integral operator (49) for $N^f \geq 100$ and thus are not included in (c) to (f). Flow is from left to right.

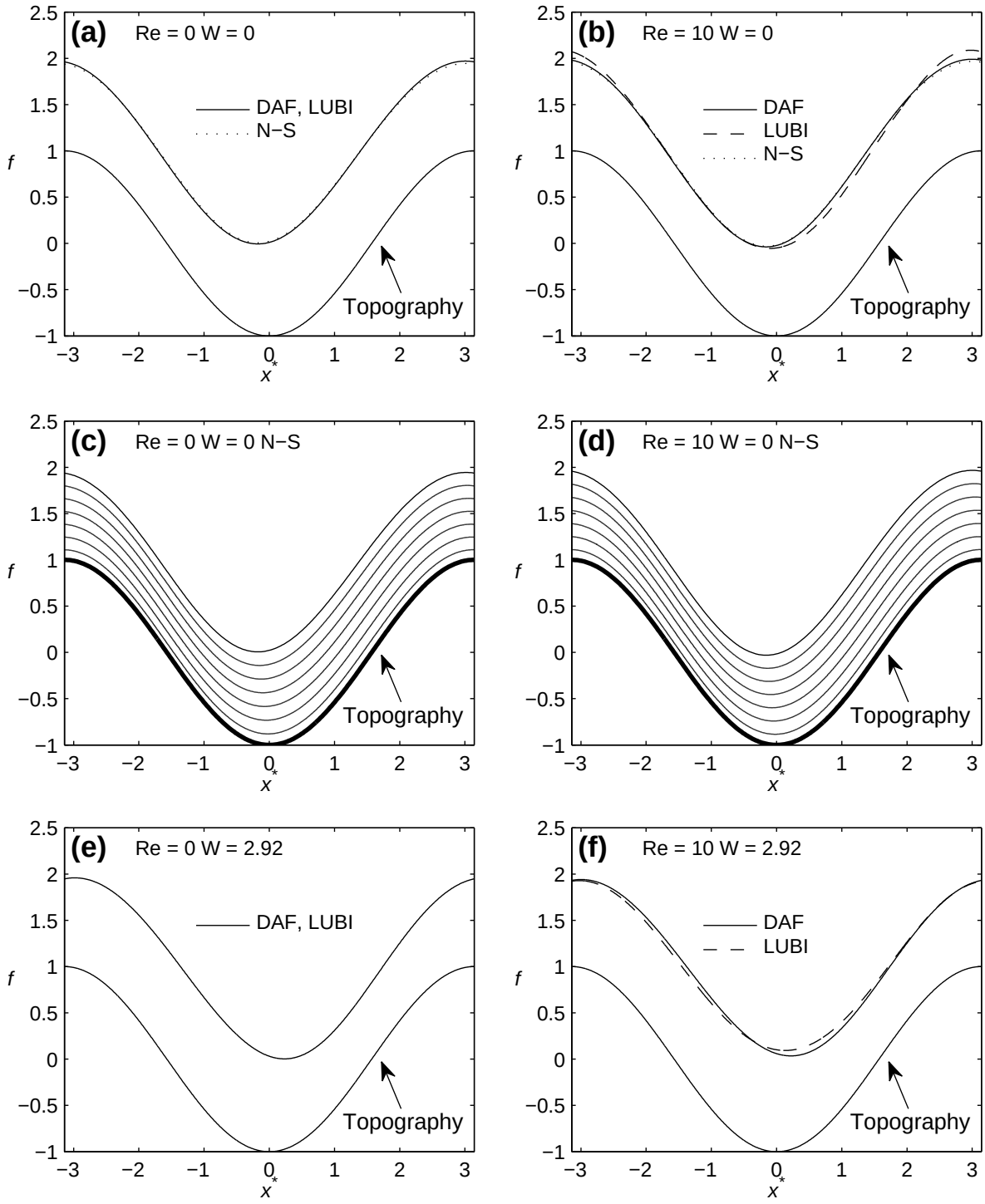

Figure 4: Film flow over a spanwise sinusoidally varying topography ($\theta = 30°$, wavelength $l_p = 2\pi$, amplitude $s_0 = 1.0$). Comparison between LUBI, DAF and N-S predictions: (a), (c), (e) Re = 0; (b), (d), (f) Re = 10; (a), (b), (c), (d) $\mathcal{W} = 0$; (e), (f) $\mathcal{W} = 2.92$; (a), (b), (e), (f) free-surface disturbance; (c), (d) streamlines showing the internal flow structure. Flow is from left to right.

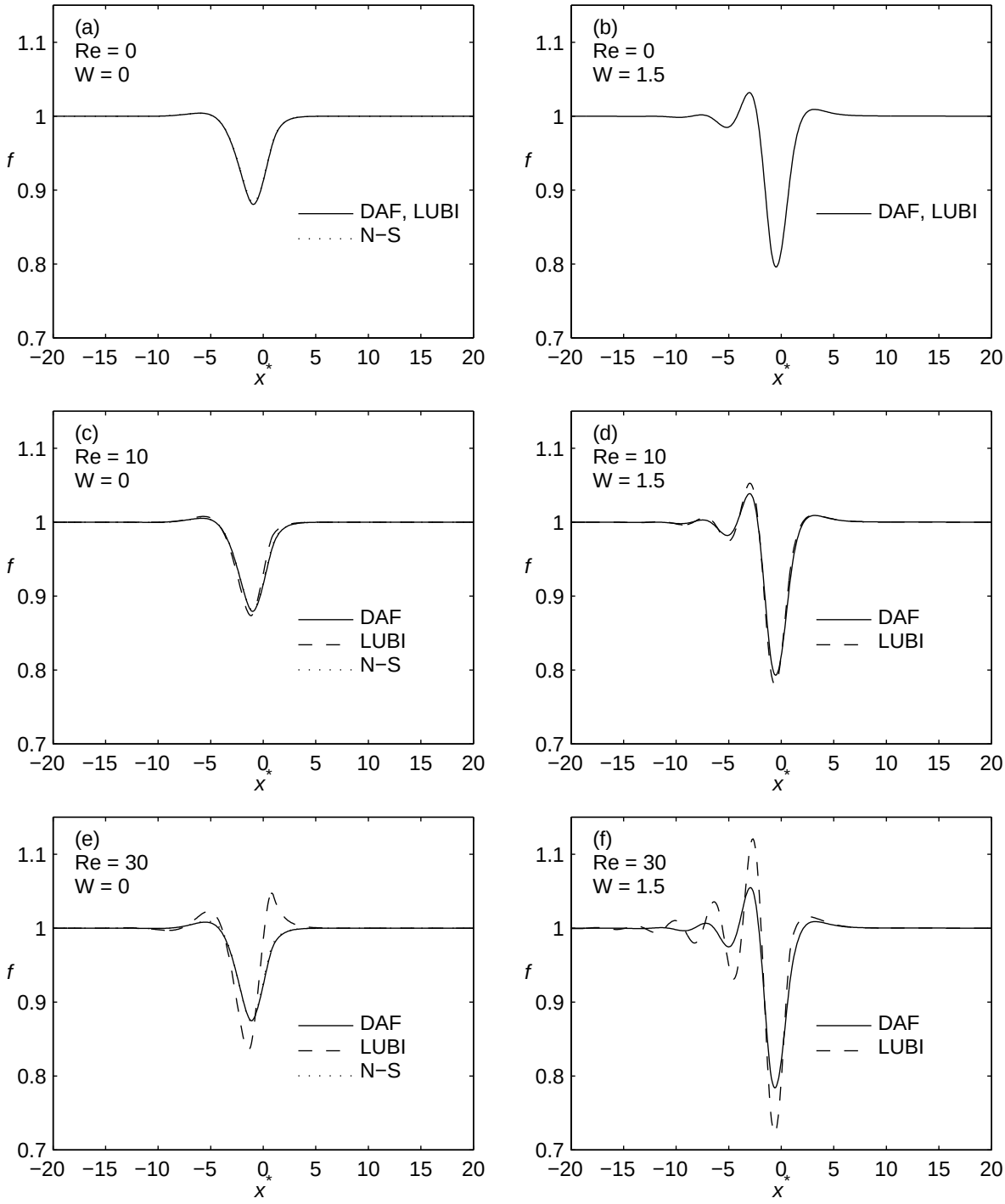

Figure 5: Free-surface disturbance for film flow over a spanwise narrow trench ($\theta = 2°$, $l_t = 2$ and $|s_0| = 0.25$), see also Figure 3. Comparison between LUBI, DAF and N-S predictions: (a), (b) Re $= 0$; (c), (d) Re $= 10$; (e), (f) Re $= 30$; (a), (c), (e) $\mathcal{W} = 0$; (b), (d), (f) $\mathcal{W} = 1.5$. Flow is from left to right.

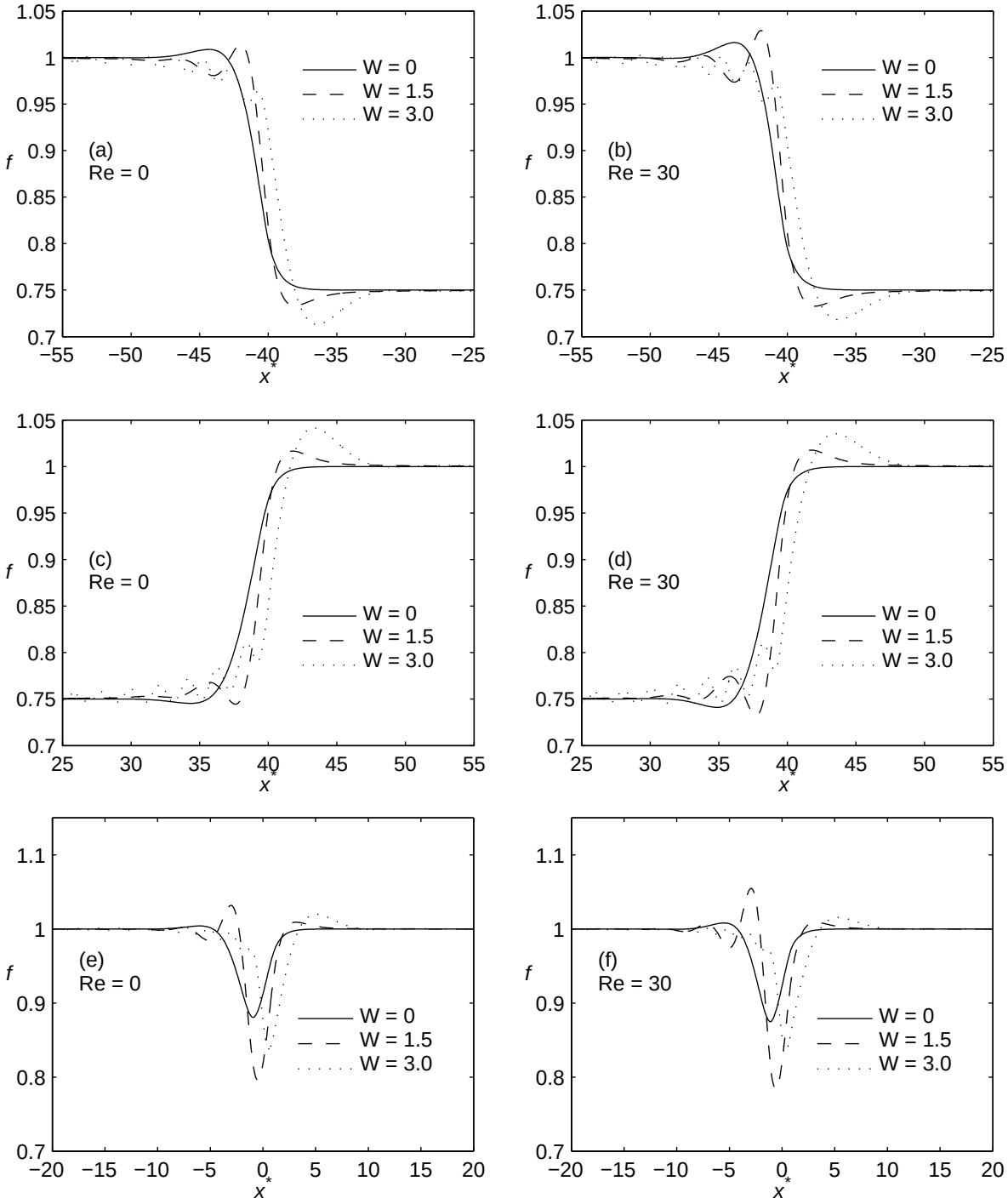

Figure 6: Free-surface profiles for electrified film flow ($\mathcal{W} = 0, 1.5, 3.0$), Re $= 0$ (left) and Re $= 30$ (right) over: (a), (b) the step-down and (c), (d) step-up part of a wide spanwise wide trench ($\theta = 2^\circ$, $l_t = 80$ and $|s_0| = 0.25$); (e), (f) the spanwise narrow trench of Figure 5 ($\theta = 2^\circ$, $l_t = 2$ and $|s_0| = 0.25$). Flow is from left to right.

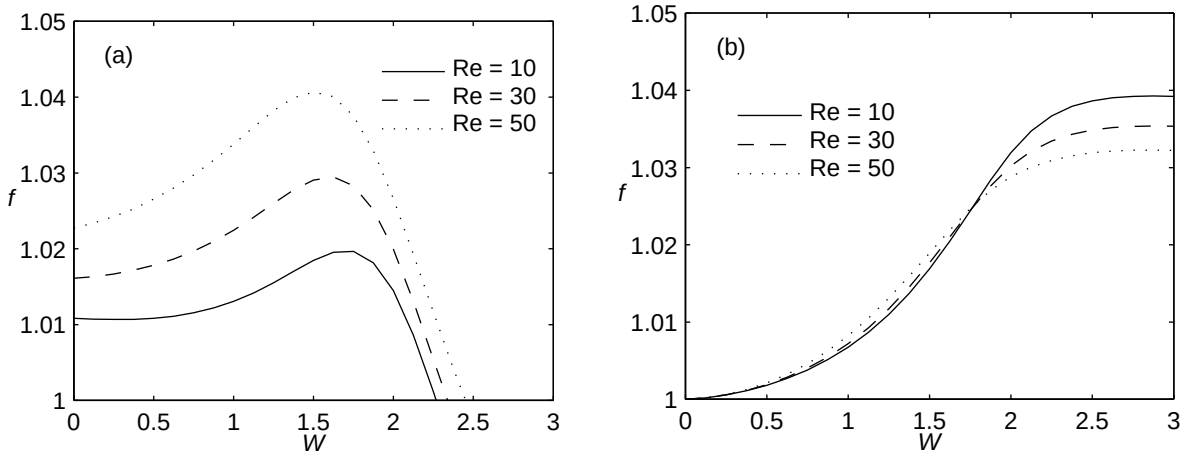

Figure 7: The effect of electric field strength and Re on the maximum values of the capillary ridge and free-surface hump for thin film flow over (a) the step-down and (b) the step-up part of the spanwise wide trench as per Figure 6 ($\theta = 2^\circ$, $l_t = 80$ and $|s_0| = 0.25$); $\mathcal{W} \in [0, 3.0]$ and Re = 10, 30 and 50.

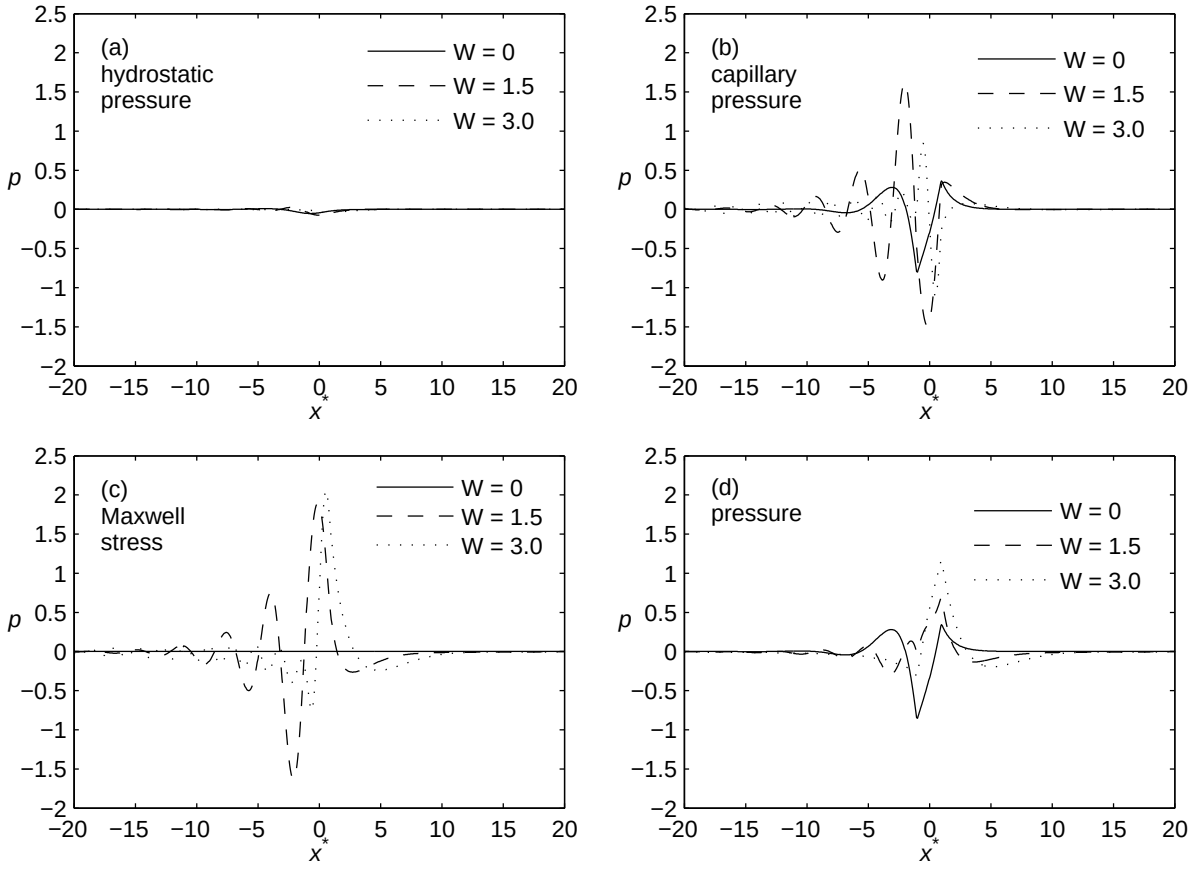

Figure 8: Contributions to the overall pressure for different electric field strengths, $\mathcal{W} = 0$, 1.5 and 3.0, when $\mathrm{Re} = 0$, for thin film flow over the spanwise narrow trench ($\theta = 30°$, $l_t = 2$ and $|s_0| = 0.25$): (a) hydrostatic pressure; (b) capillary pressure; (c) Maxwell stress; (d) overall pressure. Flow is from left to right.

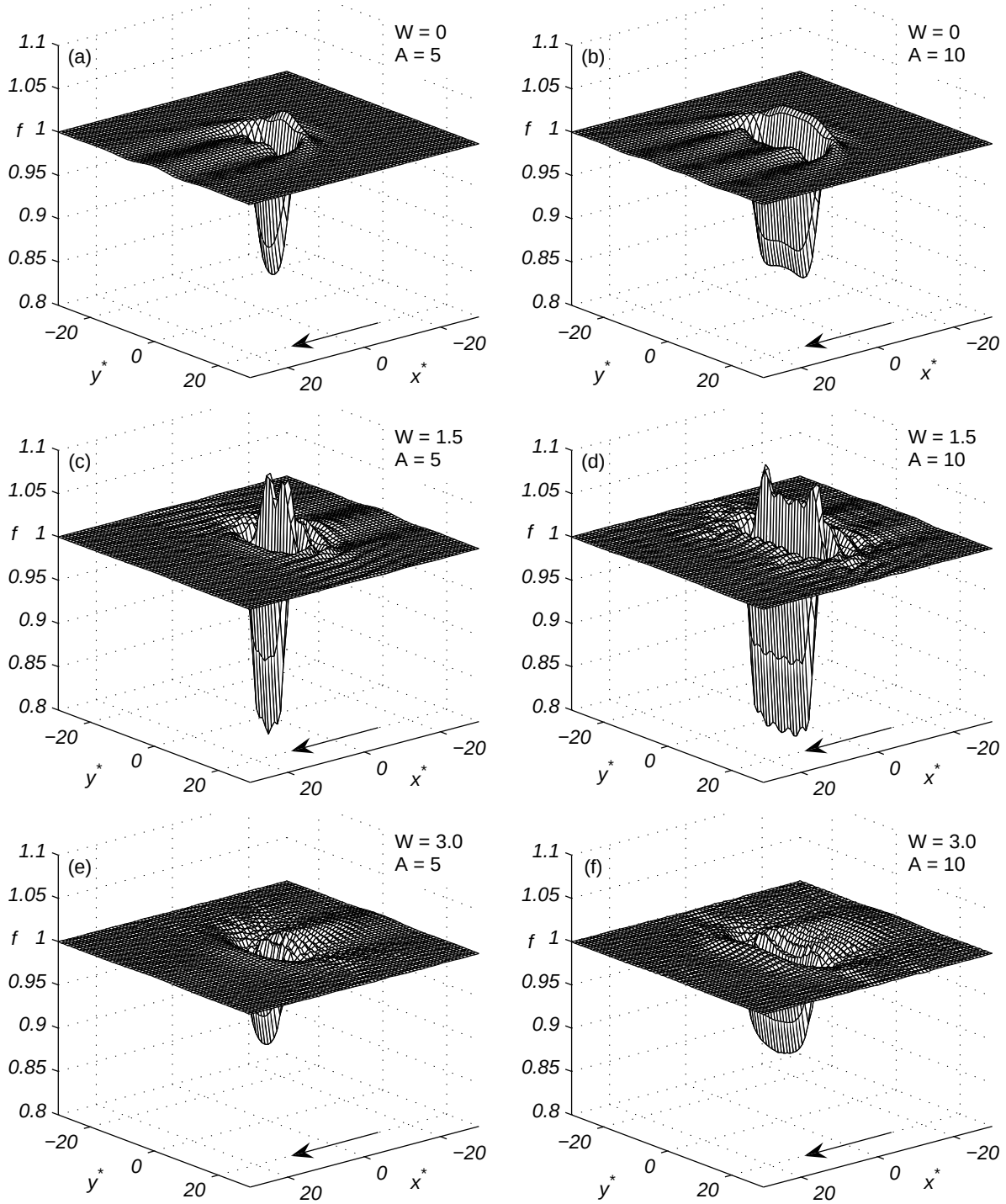

Figure 9: Plots of the free-surface disturbance resulting from film flow, Re = 0, over a localised rectangular trench topography ($\theta = 30°$, $l_t = 2$ and $|s_0| = 0.25$), showing the effect of aspect ratio, $A = w_t/l_t$. From top to bottom, $\mathcal{W} = 0, 1.5, 3.0$; $A = 5$ (left) and $A = 10$ (right). The arrow indicates the direction of flow.

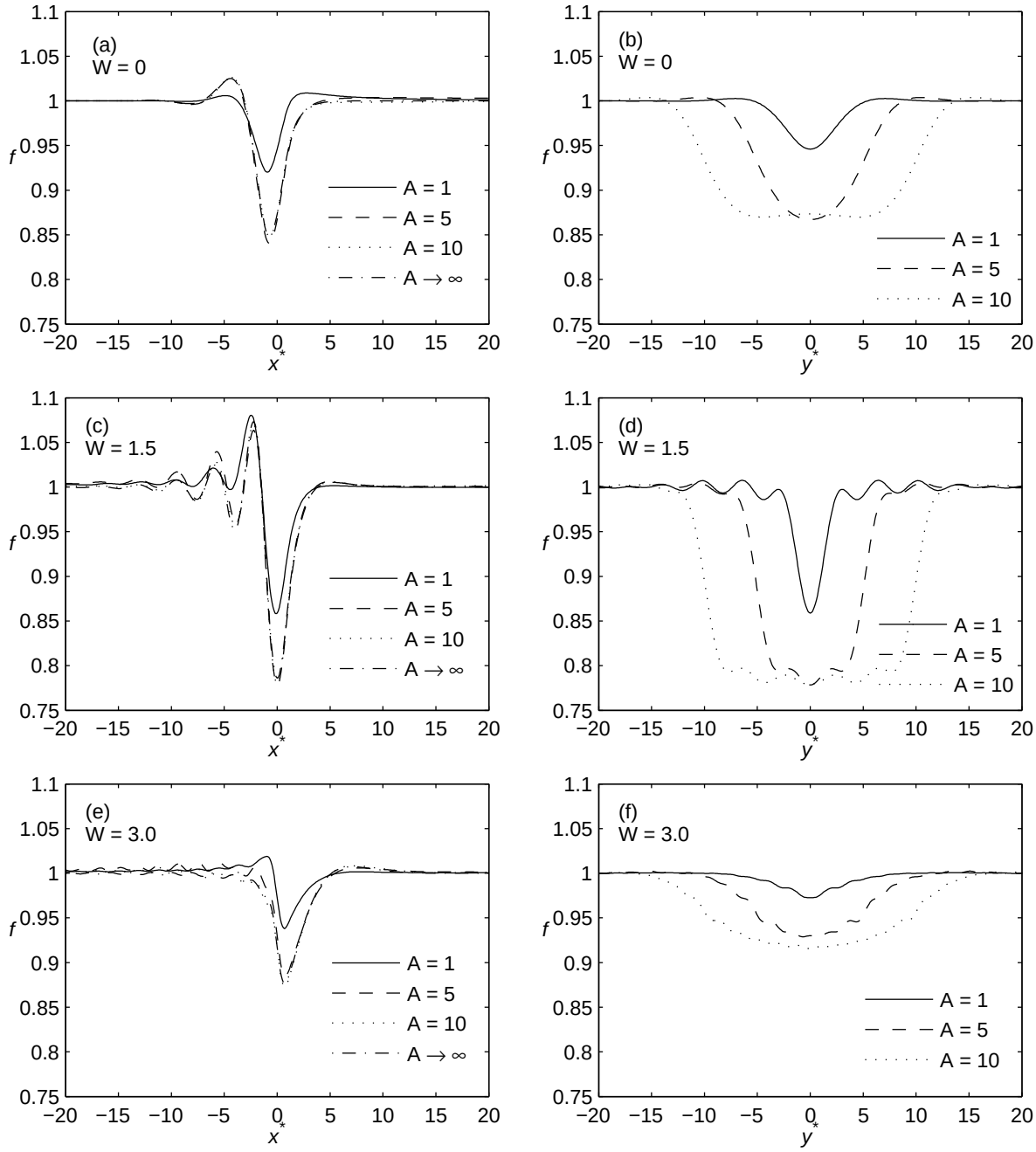

Figure 10: Streamwise (left) and spanwise (right) free-surface profiles through the centre of the localised rectangular trench topography of Figure 9, showing the effect of aspect ratio, $A = w_t/l_t$. From top to bottom, $\mathcal{W} = 0, 1.5, 3.0$. The streamwise profile for the corresponding spanwise flow is shown for comparison purposes and labelled $A \to \infty$.

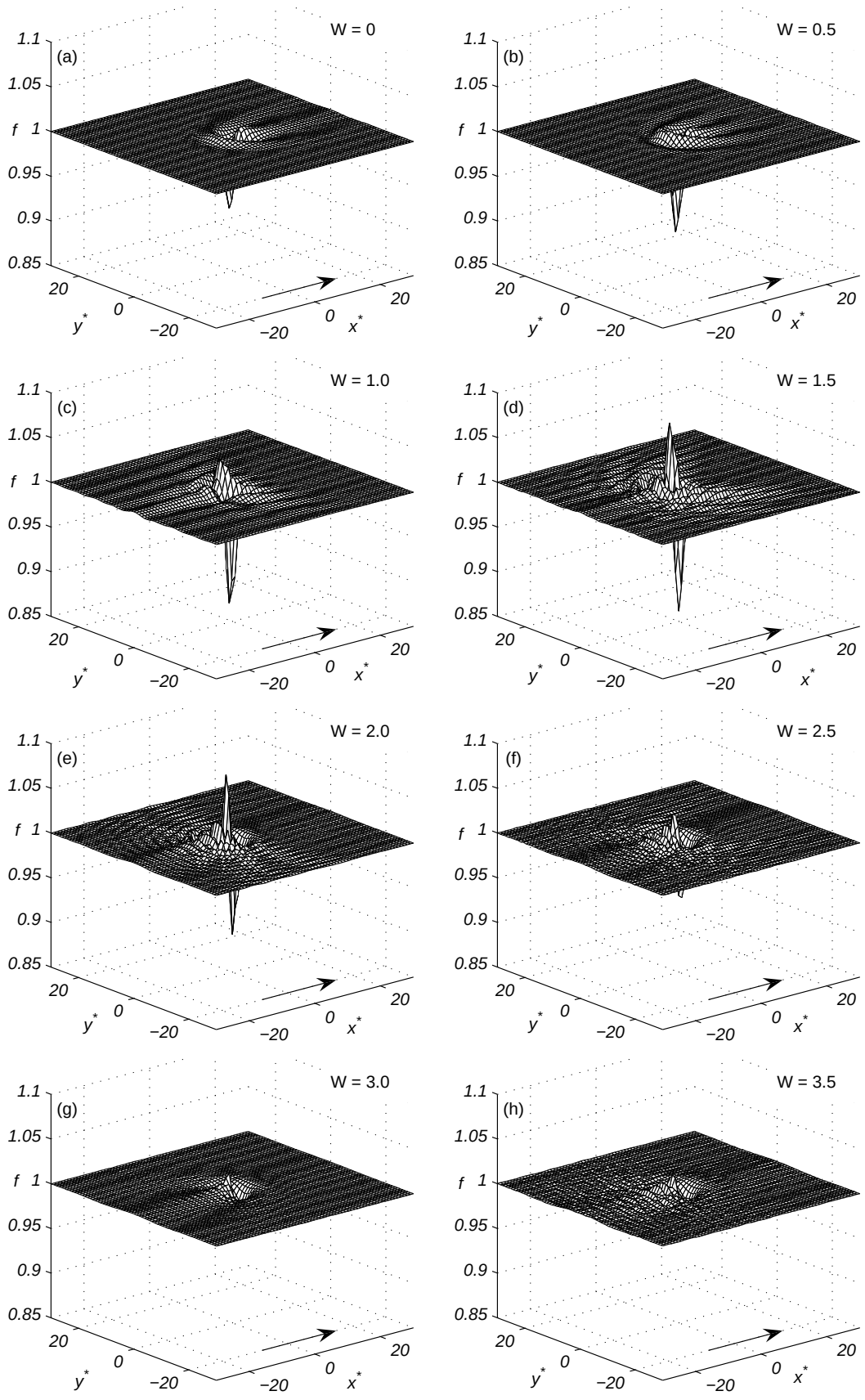

Figure 11: Plots of the free-surface disturbance resulting from film flow, Re = 0, over a localised square trench topography, $\theta = 30°$, $l_t = w_t = 2$ and $|s_0| = 0.25$: $\mathcal{W}$ = (a) 0, (b) 0.5, (c) 1.0, (d) 1.5, (e) 2.0, (f) 2.5, (g) 3.0 and (h) 3.5. The arrow indicates the direction of flow.

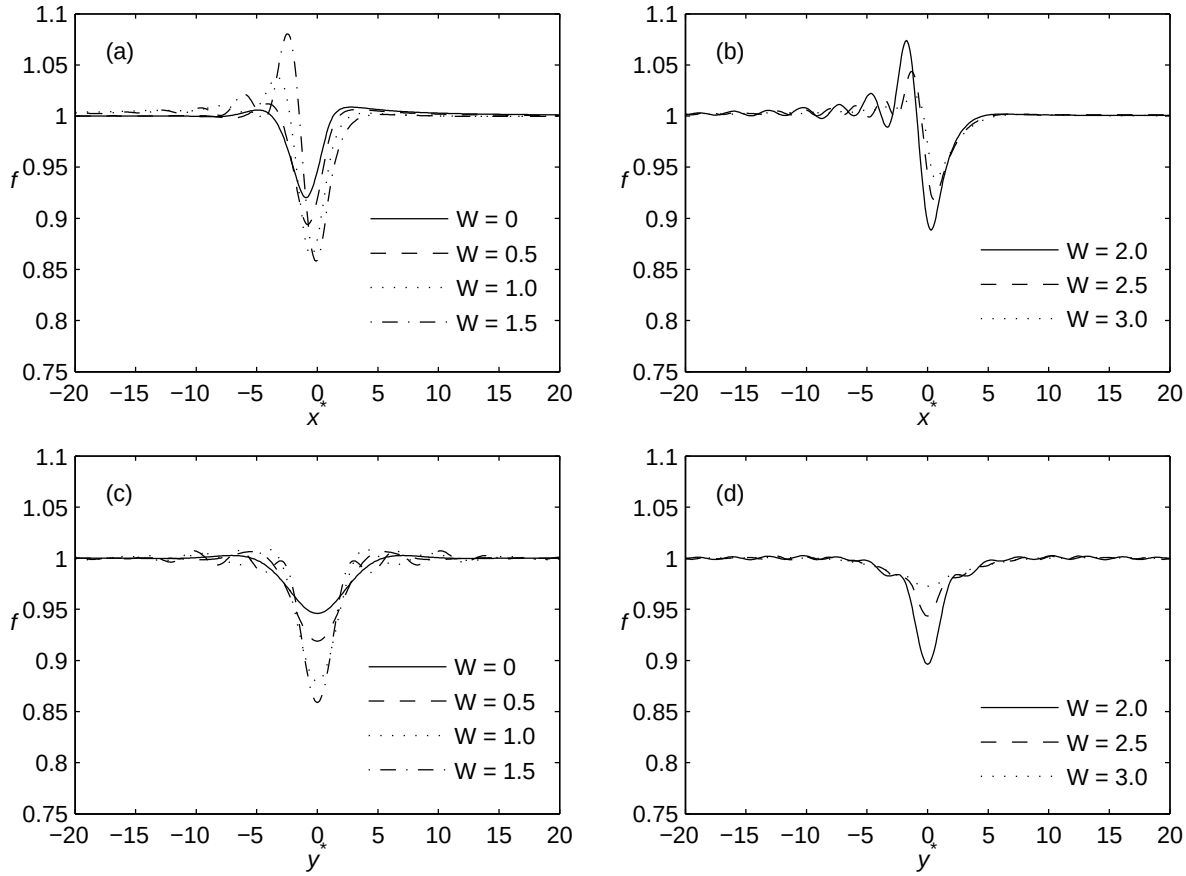

Figure 12: Streamwise (top) and spanwise (bottom) free-surface profiles through the centre of the localised square trench topography of Figure 11: (a), (c) $\mathcal{W} = 0$, 0.5, 1.0 and 1.5; (b), (d) $\mathcal{W} = 2.0$, 2.5 and 3.0.

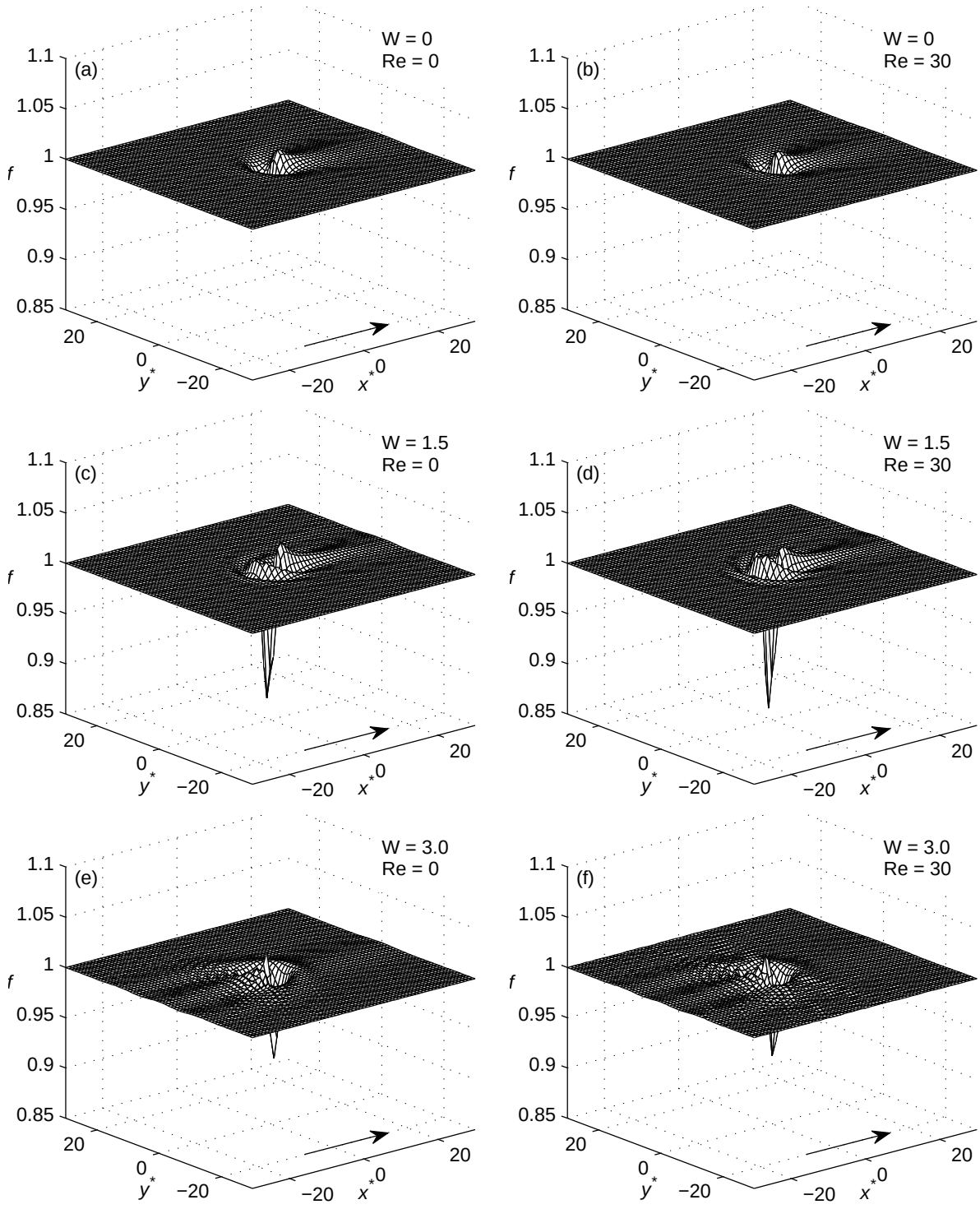

Figure 13: Plots of the free-surface disturbance resulting from film flow over a localised square trench topography, $\theta = 2°$, $l_t = w_t = 2$ and $|s_0| = 0.25$: from top to bottom, $\mathcal{W} = 0, 1.5, 3.0$; $\mathrm{Re} = 0$ (left) and $\mathrm{Re} = 30$ (right). The arrow indicates the direction of flow.

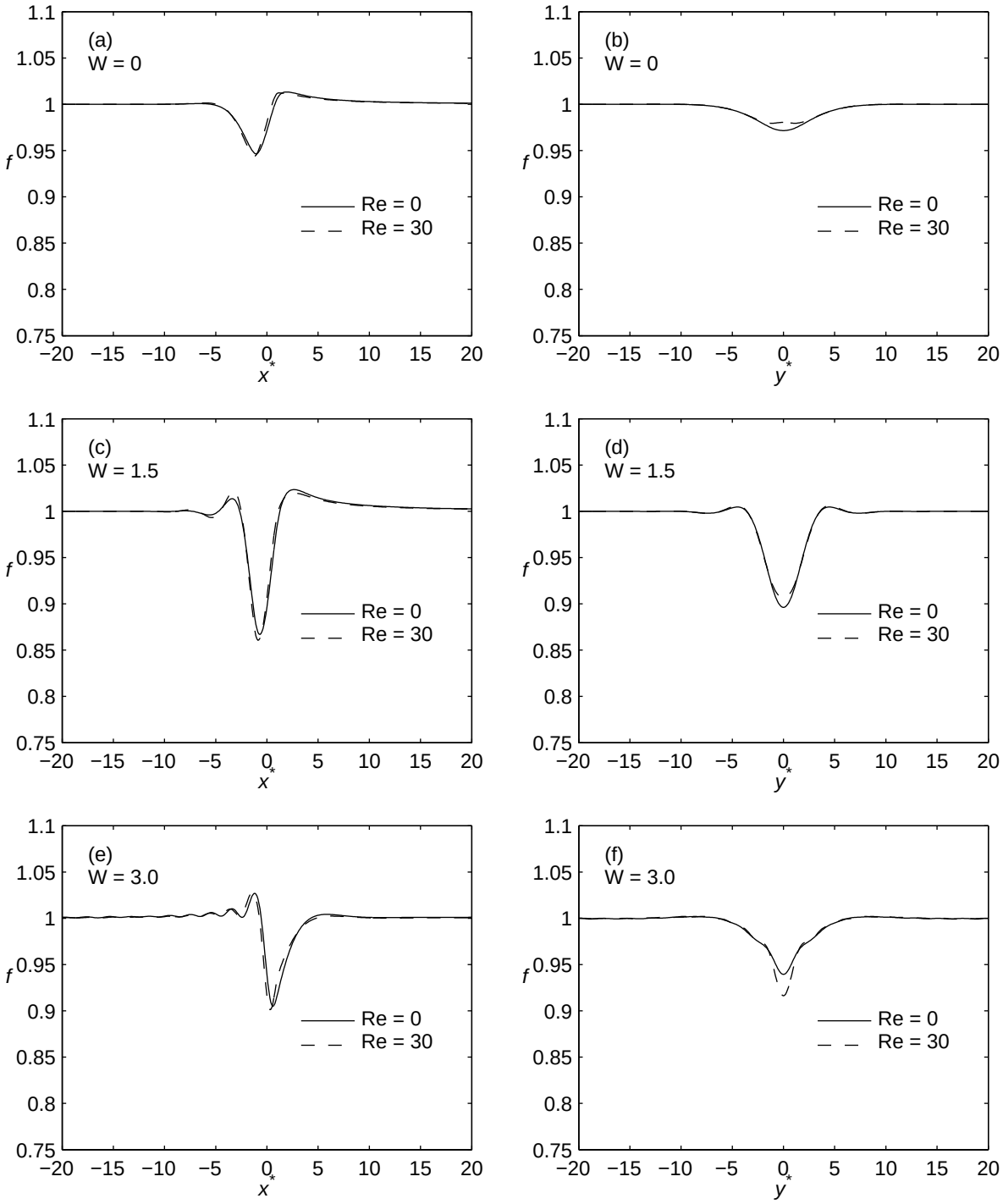

Figure 14: Streamwise (left) and spanwise (right) free-surface profiles through the centre of the localised square trench topography of Figure 13, showing the effect of changing Re from 0 to 30. From top to bottom, $\mathcal{W} = 0$, 1.5, 3.0.

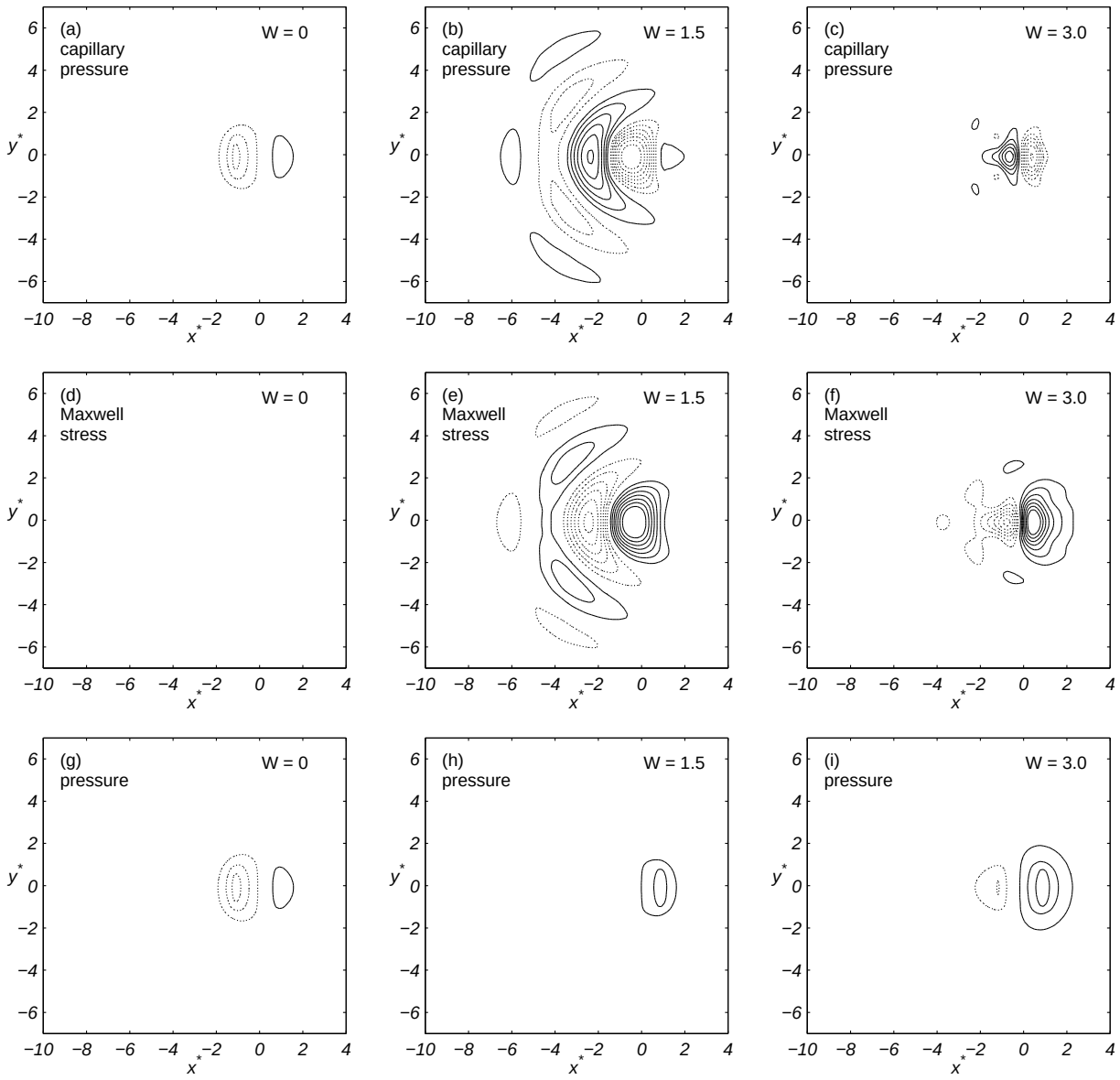

Figure 15: Pressure budget contour plots for thin film flow, Re = 0, over the localised square trench topography of Figure 11: (a), (b), (c) capillary pressure for $\mathcal{W} = 0$, 1.5, 3.0; (d), (e), (f) Maxwell stress for $\mathcal{W} = 0$, 1.5, 3.0; (g), (h), (i) overall pressure for $\mathcal{W} = 0$, 1.5, 3.0. Contour values are chosen to be equal in magnitude but opposite in sign $|p| = 0.2$,0.4,0.6,0.8,1.0,1.2,1.4. Negative contour values are indicated as dotted lines. Hydrostatic pressure is not plotted since its modulus is less than the smallest contour value. The direction of flow is from left to right.

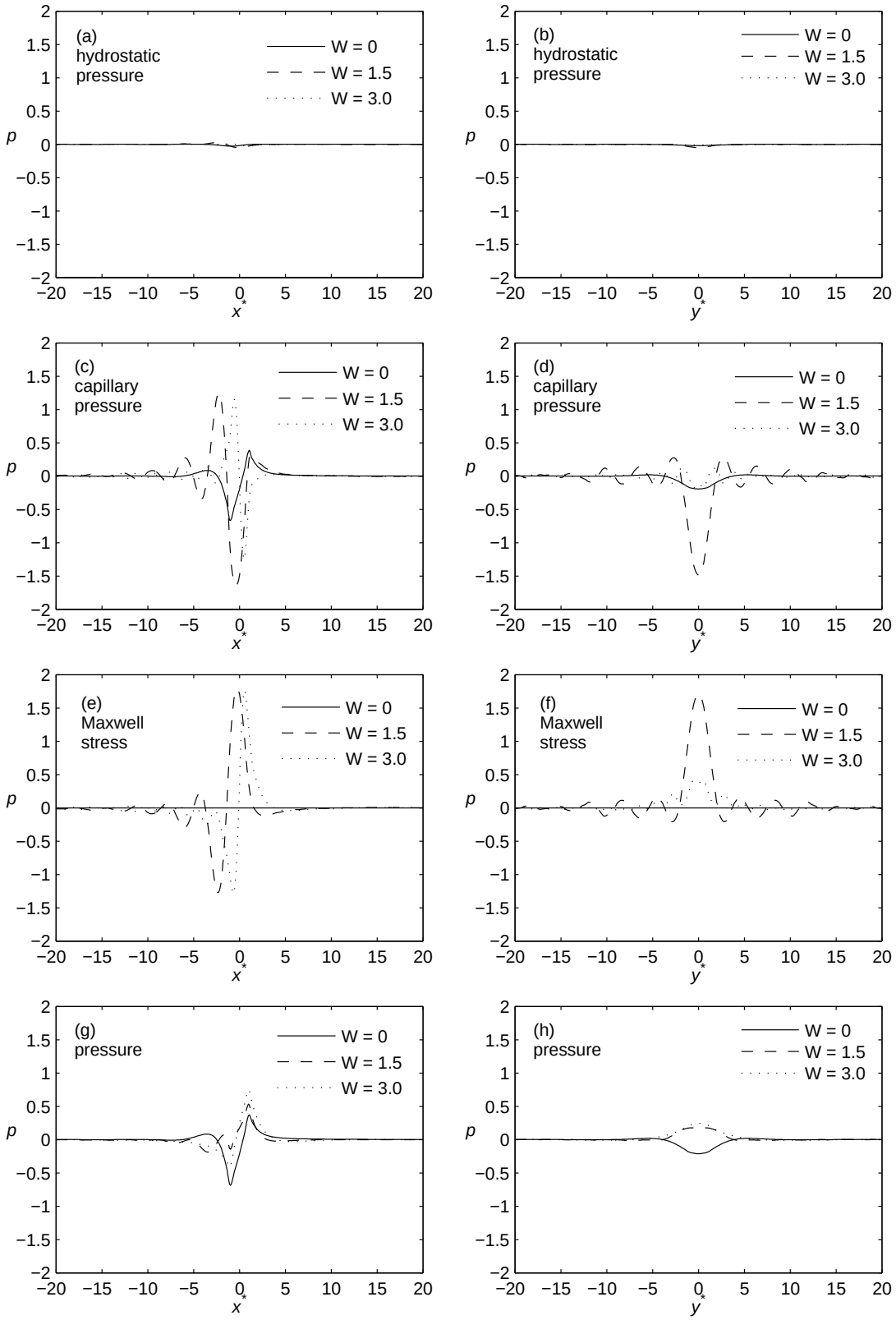

Figure 16: Streamwise (left) and spanwise (right) pressure budget profiles through the centre of the localised square trench topography of Figure 11, Re = 0: (a), (b) hydrostatic pressure; (c), (d) capillary pressure; (e), (f) Maxwell stress; (g), (h) overall pressure. Comparison is made for $\mathcal{W} = 0$, 1.5 and 3.0.

References

[1] Anderson, E., Bai, Z., Bischof, C., Blackford, S., Demmel, J., Dongarra, J., Du Croz, J., Greenbaum, A., Hammarling, S., Mckenney, A., Sorensen, D., 1999 LAPACK users' guide. Society for Industrial and Applied Mathematics

[2] Argyriadi, K., Vlachogiannis, M., Bontozoglou, V., 2006 Experimental study of inclined film flow along periodic corrugations: the effect of wall steepness. Phys. Fluids 18, Art. No. 012102.

[3] Bankoff, S.G., Miksis, M.J., Gwinner, H., Kim, R., 1994 Design considerations for the rotating electrostatic liquid-film radiator. Nucl. Engng. Des. 149, 441-447.

[4] Bankoff, S.G., Griffing, E.M., Schluter, R.A., 2002 Use of an electric field in an electrostatic liquid film radiator. Ann. N.Y. Acad. Sci. 974, 1-9.

[5] Baxter, S.J., Power, H., Cliffe, K.A., Hibberd, S., 2009 Three-dimensional thin film flow over and around an obstacle on an inclined plane. Phys. Fluids 21(3), Art. No. 032102.

[6] Baxter, S.J., Power, H., Cliffe, K.A., Hibberd, S., 2010 Free surface Stokes flows obstructed by multiple obstacles. Int. J. Numer. Meth. Fl. 62(5), 530-564.

[7] Benjamin, T.B., 1957 Wave formation in laminar flow down an inclined plane. J. Fluid Mech. 2, 554-574.

[8] Benney, D.J., 1966 Long waves in liquid films. J. Math. Phys. 45(2), 150-155.

[9] Bertozzi, A.L., Brenner, M.P., 1997 Linear stability and transient growth in driven contact lines. Phys. Fluids 9(3), 530-539.

[10] Blyth, M.G., Pozrikidis, C., 2006 Film flow down an inclined plane over a three-dimensional obstacle. Phys. Fluids 18(5), Art. No. 052104.

[11] Blyth, M.G. 2010. Private communication.

[12] Bontozoglou, V., Serifi, K., 2008 Falling film flow along steep two-dimensional topography: The effect of inertia. Int. J. Multiphas. Flow 34(8), 734-747.

[13] Chang, H.C., 1986 Traveling waves on fluid interfaces: Normal form analysis of the Kuramoto-Sivashinsky equation. Phys. Fluids 29(10), 3142-3147.

[14] Chang, H.C., 1994 Wave evolution on a falling film. Ann. Rev. Fluid Mech. 26, 103-136.

[15] Chung, T.J., 2002 Computational fluid dynamics. Cambridge University Press.

[16] Craster, R.V., Matar, O.K., 2005 Electrically induced pattern formation in thin leaky dielectric films. Phys. Fluids 17, Art. No. 032104.

[17] Craster, R.V., Matar, O.K., 2009 Dynamics and stability of thin liquid films. Rev. Mod. Phys 81, 1131-1198.

[18] Dávalos-Orozco, L.A., 2007 Nonlinear instability of a thin film flowing down a smoothly deformed surface. Phys. Fluids 19, Art. No. 074103.

[19] Dávalos-Orozco, L.A., 2008 Instabilities in thin films flowing down flat and smoothly deformed walls. Microgravity Sci. Tech. 20, 225-229.

[20] D'Alessio, S.J.D., Pascal, J.P., Jasmine, H.A., 2009 Instability in gravity-driven flow over uneven surfaces, Phys. Fluids 21, Art. No. 062105.

[21] Decré, M.M.J., Baret, J.C., 2003 Gravity-driven flows of viscous liquids over two-dimensional topographies. J. Fluid Mech. 487, 147-166.

[22] Gaskell, P.H., Jimack, P.K., Sellier, M., Thompson, H.M., Wilson, M.C.T., 2004 Gravity-driven flow of continuous thin liquid films on non-porous substrates with topography. J. Fluid Mech. 509, 253-280.

[23] Gaskell, P.H., Jimack, P.K., Sellier, M., Thompson, H.M., 2006 Flow of evaporating, gravity-driven thin liquid films over topography. Phys. Fluids 18(1), Art. No. 013601.

[24] González, A., Castellanos, A., 1996 Nonlinear electrohydrodynamic waves on films falling down an inclined plane. Phys. Rev. E 53(4), 3573-3578.

[25] Gramlich, C.M., Kalliadasis, S., Homsy, G.M., Messer, C., 2002 Optimal leveling of flow over one-dimensional topography by Marangoni stresses. Phys. Fluids 14(6), 1841-1850.

[26] Gray, N.F., 2008 Drinking Water Quality: Problems and Solutions. 2nd Edition. Cambridge University Press.

[27] Griffing, E.M., Bankoff, S.G., Miksis, M.J., Schluter, R.A., 2006 Electrohydrodynamics of thin flowing films. J. Fl. Eng.-Trans. ASME 128(2), 276-283.

[28] Gu, F., Liu, C.J., Yuan, X.G., Yu, G.C., 2004 CFD simulation of liquid film flow on inclined plates. Chem. Engng. Technol. 27, 1099-1104.

[29] Häcker, T., Uecker, H., 2009 An integral boundary layer equation for film low over inclined wavy bottoms. Phys. Fluids 21, Art. No. 092105.

[30] Heining, C., Aksel, N., 2009 Bottom reconstruction in thin-film flow over topography: Steady solution and linear stability. Phys. Fluids 21(8), Art. No. 083605.

[31] Helbig, K., Alexeev, A., Gambaryan-Roisman, T., Stephan, P., 2005 Evaporation of falling and shear-driven thin films on smooth and grooved surfaces. Flow Turbul. Combust. 75(1-4), 85-104.

[32] Helbig, K., Nasarek, R., Gambaryan-Roisman, T., Stephan, P., 2009 Effect of longitudinal minigrooves on flow stability and wave characteristics of falling liquid films. J. Heat Trans.-T. ASME 131(1), 011601.

[33] Kalliadasis, S., Bielarz, C., Homsy, G.M., 2000 Steady free-surface thin film flows over topography. Phys. Fluids 12(8), 1889-1898.

[34] Kelley, C.T., 2003 Solving Nonlinear Equations with Newton's Method. SIAM.

[35] Kim, H., Bankoff, S.G., Miksis, M.J., 1992 The effect of an electrostatic field on film flow down an inclined plane. Phys. Fluids A 4(10), 2117-2130.

[36] Kistler, S.F., Schweizer, P.M. editors, 1997 Liquid Film Coating. Chapman and Hall.

[37] Kuffel, E., Zaengl, W.S., Kuffel, J., 2000 High Voltage Engineering. Butterworth-Heinemann.

[38] Landau, L.D., Lifshitz, E.M., 1984 Electrodynamics of Continuous Media. Pergamon.

[39] Lin, S.P., 1974 Finite amplitude side-band stability of a viscous film. J. Fluid Mech. 63(3), 417-429.

[40] Liu, J., Paul, J.D., Gollub, J.P., 1993 Measurements of the primary instabilities of film flows. J. Fluid Mech. 250, 69-101.

[41] Liu, J., Gollub, J.P., 1994 Solitary wave dynamics of film flows. Phys. Fluids 6, 1702-1712.

[42] Luo, H.X., Pozrikidis, C., 2006 Effect of inertia on film flow over oblique and three-dimensional corrugations. Phys. Fluids 18(12), Art. No. 078107.

[43] Luo, H., Pozrikidis, C., 2007 Gravity-driven film flow down an inclined wall with three-dimensional corrugations. Acta Mech. 188(3-4), 209-225.

[44] Mahlmann, S., Papageorgiou, D.T., 2009 Numerical study of electric field effects on the deformation of two-dimensional liquid drops in simple shear flow at arbitrary Reynolds number. J. Fluid Mech. 626, 367-393.

[45] Malamataris, N.A., Bontozoglou, V., 1999 Computer aided analysis of viscous film flow along an inclined wavy wall. J. Comput. Phys. 154(2), 372-392.

[46] Malamataris, N.A., Vlachogiannis, M., Bontozoglou, V., 2002 Solitary waves on inclined films: Flow structure and binary interactions. Phys. Fluids 14(3), 1082-1094.

[47] Mazouchi, A., Homsy, G.M., 2001 Free surface Stokes flow over topography. Phys. Fluids 13(10), 2751-2761.

[48] Meek, J.M., Craggs, J.D., 1978 Electrical Breakdown of Gases. John Wiley and Sons.

[49] Melcher, R.J., Taylor, G.I., 1969 Electrohydrodynamics: a review of the role of interfacial shear stresses. Annu. Rev. Fluid Mech. 1, 111-146.

[50] Nakajima, K., Miyamoto, K., 1993 Coating Method. European patent 0,530,752 A1.

[51] Nakaya, C., 1975 Long waves on a thin fluid layer flowing down an inclined plane. Phys. Fluids 18(11), 1407-1412.

[52] Nguyen, P.-K., Bontozoglou, V., 2011 Steady solutions of inertial film flow along strongly undulated substrates, Phys. Fluids 23, Art. No. 052103.

[53] Oddy, M.H., Santiago, J.G., Mikkelsen, J.C., 2001 Electrokinetic instability micromixing. Anal. Chem. 73, 5822-5832.

[54] Oron, A., Davis, S.H., Bankoff, S.G., 1997 Long-scale evolution of thin liquid films. Rev. Mod. Phys. 69(3), 931-980.

[55] Peurrung, L.M., Graves, D.B., 1993 Spin coating over topography. IEEE Trans. Semicond. Manu. 6, 72-76.

[56] Pozrikidis, C., 1988 The flow of a liquid film along a periodic wall. J. Fluid Mech. 188, 275-300.

[57] Pozrikidis, C., Thoroddsen, S.T., 1991 The deformation of a liquid-film flowing down an inclined plane wall over a small particle arrested on the wall. Phys. Fluids 3(11), 2546-2558.

[58] Ramaswamy, B., Chippada, S., Joo, S.W., 1996 A full-scale numerical study of interfacial instabilities in thin-film flows. J. Fluid Mech. 325, 163-194.

[59] Saprykin, S., Koopmans, R.J., Kalliadasis, S., 2007 Free-surface thin-film flows over topography: influence of inertia and viscoelasticity. J. Fluid Mech. 578, 271-293.

[60] Schäffer, E., Thurn-Albrecht, T., Russel, T.P., Steiner, U., 2000 Electrically induced structure formation and pattern transfer. Nature 403, 874-877.

[61] Scholle, M., Haas, A., Aksel, N., Wilson, M.C.T., Thompson, H.M., Gaskell, P.H., 2008a Competing geometric and inertial effects on local flow structure in thick gravity-driven fluid films. Phys. Fluids 20(12), Art. No. 123101.

[62] Scholle, M., Haas, A., Aksel, N., Thompson, H.M., Hewson, R.W., Gaskell, P.H., 2008b The effect of locally induced flow structure on global heat transfer for plane laminar shear flow. Int. J. Heat Fluid Fl. 30, 175-185.

[63] Scholle, M., Haas, A., Aksel, N., Wilson, M.C.T., Thompson, H.M., Gaskell, P.H., 2009 Eddy genesis and manipulation in plane laminar shear flow. Phys. Fluids 21(7), Art. No. 073602.

[64] Sellier, M., 2008 Substrate design or reconstruction from free surface data for thin film flows. Phys. Fluids 20(6), Art. No. 062106.

[65] Serifi, K., Malamataris, N.A., Bontozoglou, V., 2004 Transient flow and heat transfer phenomena in inclined wavy films. Int. J. Therm. Sci. 43(8), 761-767.

[66] Shkadov, V.Y., 1967 Wave flow regimes of a thin layer of viscous fluid subject to gravity. Izv. Akad. Nauk SSSR Fluid Dynamics 2(1), 29-34.

[67] Shkadov, V.Y., 1968 Wave-flow theory for a thin viscous liquid layer. Izv. Akad. Nauk SSSR Fluid Dynamics 3(2), 12-15.

[68] Snir, M., Otto, S.W., Huss-Lederman, S., Walker, D.W., Dongarra, J., 1996 MPI: The Complete Reference. The MIT Press.

[69] Spurk, J.H., Aksel, N., 2008 Fluid Mechanics. Springer.

[70] Stillwagon, L.E., Larson, R.G., 1988 Fundamentals of topographic substrate leveling. J. App. Phys 63(11), 5251-5258.

[71] Stillwagon, L.E., Larson, R.G., 1990 Leveling of thin-films over uneven substrates during spin coating. Phys. Fluids 2(11), 1937-1944.

[72] Tabeling, P., 2005 Introduction to Microfluidics. Oxford University Press.

[73] Trifonov, Y.Y., 1999 Viscous liquid film flows over a periodic surface. Int. J. Multiphas. Flow 24(7), 1139-1161.

[74] Trifonov, Y.Y., 2004 Viscous film flow down corrugated surfaces. J. Appl. Mech. Tech. Phys. 45(3), 389-400.

[75] Trifonov, Y.Y., 2007 Stability of a viscous liquid film flowing down a periodic surface. Int. J. Multiphas. Flow 33, 1186-1204.

[76] Trottenberg, U., Oosterlee, C.W., Schüller, A., 2001 Multigrid. Academic Press.

[77] Tseluiko, D., Papageorgiou, D.T., 2006a Wave evolution on electrified falling films. J. Fluid Mech. 556, 361-386.

[78] Tseluiko, D., Papageorgiou, D.T., 2006b Nonlinear dynamics of electrified thin liquid films. Siam J. Appl. Math. 67(5), 1310-1329.

[79] Tseluiko, D., Blyth, M.G., Papageorgiou, D.T., Vanden-Broeck, J.M., 2008a Electrified viscous thin film flow over topography. J. Fluid Mech. 597, 449-475.

[80] Tseluiko, D., Blyth, M.G., Papageorgiou, D.T., Vanden-Broeck, J.M., 2008b Effect of an electric field on film flow down a corrugated wall at zero Reynolds number. Phys. Fluids 20(4), Art. No. 042103.

[81] Tseluiko, D., Blyth, M.G., 2009 Effect of inertia on electrified film flow over a wavy wall. J. Eng. Math. 65(3), 229-242.

[82] Veremieiev, S., Thompson, H.M., Lee, Y.C., Gaskell, P.H., 2010 Inertial thin film flow on planar surfaces featuring topography. Comp., Fluids 39(3), 431-450.

[83] Veremieiev, S., 2011 Gravity-driven continuous thin film flow over topography, PhD Thesis, University of Leeds.

[84] Vlachogiannis, M., Bontozoglou, V., 2002 Experiments on laminar film flow along a periodic wall. J. Fluid Mech. 457, 133-156.

[85] Weinstein, S.J., Ruschak, K.J., 2004 Coating Flows. Ann. Rev. Fluid Mech. 36, 29-53.

[86] Wierschem, A., Aksel, N., 2003 Instability of a liquid film flowing down an inclined wavy plane. Physica D 186, 221-237.

[87] Wierschem, A., Scholle, M., Aksel, N., 2003 Vortices in film flow over strongly undulated bottom profiles at low Reynolds numbers. Phys. Fluids 15(2), 426-435 (2003).

[88] Wierschem, A., Aksel, N., 2004 Influence of inertia on eddies created in films creeping over strongly undulated substrates. Phys. Fluids 16, 4566-4574.

[89] Wierschem, A., Lepski, C., Aksel, N., 2005 Effect of long undulated bottoms on thin gravity-driven films. Acta Mech. 179(1-2), 41-66.

[90] Wierschem, A., Pollak, T., Heining, C., Aksel, N., 2010 Suppression of eddies in films over topography. Phys. Fluids 22, Art. No. 113603.

[91] Wu, N., Pease, L.F., Russel, W.B., 2005 Electric-field-induced patterns in thin polymer films: Weakly nonlinear and fully nonlinear evolution. Langmuir 21(26), 12290-12302.

[92] Yeo, L.Y., Craster, R.V., Matar, O.K., 2007 Drop manipulation and surgery using electric fields. J. Coll. Int. Sci 306, 368-378.

[93] Yih, C.S., 1963 Stability of liquid flow down an inclined plane. Phys. Fluids 6(3), 321-334.

[94] Yoshimura, P.N., Nosoko, T., Nagata, T., 1996 Enhancement of mass transfer into a falling laminar liquid film by two-dimensional surface waves: some experimental observations and modeling. Chem. Engng. Sci. 51, 1231-1240.

[95] Zhao, L., Cerro, R.L., 1992 Experimental characterization of viscous film flows over complex surfaces. Int. J. Multiphas. Flow 18(4), 495-516.